Volume 10
Number 7
7 April 2022
Pages 1599-1846

Biomaterials Science

rsc.li/biomaterials-science

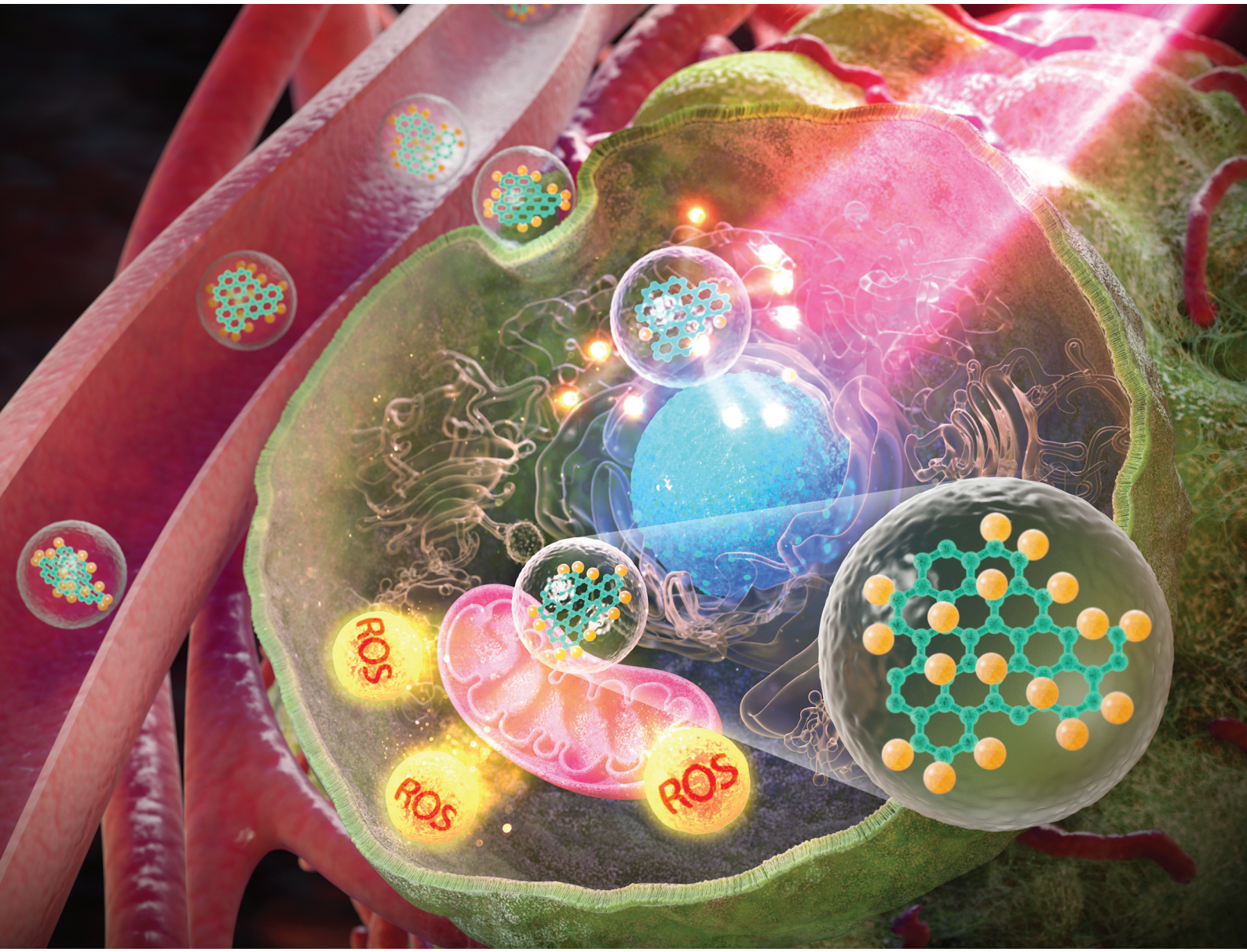

ISSN 2047-4849

PAPER

Md Moniruzzaman, Ki-Taek Lim *et al.*
Two-photon excitable membrane targeting polyphenolic carbon dots for long-term imaging and pH-responsive chemotherapeutic drug delivery for synergistic tumor therapy

ROYAL SOCIETY OF CHEMISTRY

European Society for Biomaterials

Biomaterials Science

ROYAL SOCIETY OF CHEMISTRY

PAPER

View Article Online
View Journal | View Issue

Cite this: *Biomater. Sci.*, 2022, **10**, 1680

Two-photon excitable membrane targeting polyphenolic carbon dots for long-term imaging and pH-responsive chemotherapeutic drug delivery for synergistic tumor therapy†

Sayan Deb Dutta, ‡[a] Jin Hexiu,‡[b] Jongsung Kim, [c] Sourav Sarkar,[d] Jagannath Mondal,[e] Jeong Man An,[f] Yong-kyu Lee,[e] Md Moniruzzaman*[c] and Ki-Taek Lim *[a]

Long-term dynamic tracking of cells with theranostic properties remains challenging due to the difficulty in preparing and delivering drugs by probes. Herein, we developed highly fluorescent one- and two-photon (OP and TP) excitable polyphenolic carbon quantum dots (CQDs) for excellent membrane-targeting and drug delivery properties for synergistic tumor therapy. The green-emissive CQDs (*g*-CQDs) were synthesized from a three-fold symmetric polyphenolic molecule, phloroglucinol (C_{3h}; symmetry elements: E, C_3, C_3^2, σ_h, S_3, and S_3^{-1}), in a sulfuric acid medium. Doxorubicin (Dox) was loaded onto the *g*-CQDs *via* electrostatic interaction, resulting in a loading efficiency and content of 54.62% and 323.25 μg mL^{-1}, respectively. The *g*-CQDs@Dox complex exhibited a higher rate of cell killing efficiency at both pH 5.0 and 6.5, with higher reactive oxygen species (ROS) generation due to the greater Dox accumulation in the tumor cells. In addition, TP cell imaging displayed excellent membrane-targeting properties with less photobleaching ability in tumor cells. The *in vivo* studies confirmed that the *g*-CQDs@Dox complex has higher affinity towards tumor cells, better inhibitory effects, and an absence of systemic toxicity. Therefore, our developed nanocarrier exhibited better cell imaging, drug delivery, and tumor-targeting properties, and could be used as a "smart" probe for synergistic tumor therapy.

Received 30th November 2021,
Accepted 23rd January 2022

DOI: 10.1039/d1bm01832a

rsc.li/biomaterials-science

1. Introduction

Long-term tracking of cancer cells using fluorescent probes has become indispensable owing to their poor selectivity and rapid photobleaching ability. These probes are incredibly biocompatible and therefore lack theranostic properties.[1] To some extent, one-photon (OP) bioimaging results in false fluorescence signals from the target cells because of its highly diffusive nature. Recently, two-photon (TP) bioimaging has gained significant attention in tumor imaging due to its deep penetration ability, low photodamage, and long-term dynamic tracking ability.[2] However, most of the developed imaging probes lack theranostic properties, limiting their tumor therapy application. For instance, the nucleus is one of the extensively studied organelles for the targeted delivery of nanomaterials.[3] Recently, nuclear-targeted delivery has been an effective approach in cancer chemotherapy, particularly for solid tumor treatment.[4] Various chemotherapeutic drugs, such as cisplatin (CDDP), paclitaxel (PTX), doxorubicin (Dox), and camptothecin (CPT), are often conjugated with drug delivery vehicles (DDVs) for targeted delivery to the nucleus of tumor cells.[5–7] Dox (an anthracycline drug) interacts with DNA *via* electrostatic interaction, resulting in DNA synthesis inhibition and apoptotic cell death.[8,9] Unlike traditional DDVs, which are mostly associated with cytoplasmic delivery, nuclear-targeted DDVs are highly effective owing to their superior ability to deliver drugs into the nucleus.[9] Several DDVs, such as immune-nanoparticles,[4] mesoporous silica nanoparticles (MSNPs),[10] and gold nanoparticles (AuNPs)[11,12] have been

[a]*Department of Biosystems Engineering, College of Agriculture and Life Sciences, Kangwon National University, Chuncheon-24341, Republic of Korea. E-mail: ktlim@kangwon.ac.kr*
[b]*Department of Plastic and Traumatic Surgery, Capital Medical University, Beijing-100069, Fengtai, China*
[c]*Department of Chemical and Biological Engineering, Gachon University, Seongnam-1342, Republic of Korea. E-mail: mani57chem@gachon.ac.kr*
[d]*Department of Chemistry, Pohang University of Science and Technology, Pohang, Gyungbuk-37673, Republic of Korea*
[e]*Department of Green Bioengineering, Korea National University of Transportation, Chungju-27470, Republic of Korea*
[f]*Department of Bioengineering, College of Engineering, Hanyang University, Seoul-04763, Republic of Korea*

†Electronic supplementary information (ESI) available. See DOI: 10.1039/d1bm01832a

‡These authors contributed equally to this paper.

demonstrated to deliver drugs inside the subcellular location of tumor cells. Therefore, an ideal DDV must have an enhanced permeability and retention (EPR) effect, less cytotoxic effect to chemotherapy agents, and improved nuclear delivery towards cancer therapy.[13] Moreover, DDVs with excellent drug carrier efficiency and enhanced bioimaging ability could be useful for developing personalized theranostics for cancer patients.[14,15]

Unlike conventional DDVs, CQD-based nanocarriers have gained considerable attention owing to their nanoscale size,[16] tunable optical and luminescence properties,[17,18] high aqueous solubility,[19] excellent chemical inertness,[20] and high photostability,[19] making them suitable for sensing[21] and delivery of chemotherapeutic drugs and cell imaging.[22,23] CQDs exhibit high drug and metal-binding capacity, less cytotoxicity, and good biocompatibility with cells. The nanoscale size (<10 nm) of CQDs enables their rapid uptake into the tumor tissues; however, they are also quickly removed from the circulatory system.[15,24,25] Gong *et al.* reported NP-doped carbon dots (NP-CDs) for rapid conjugation of Dox and targeted *in vivo* delivery with low cytotoxicity.[26] In another study, honeycomb-like CQDs (HC-CQDs) were developed to deliver multiple drugs to regulate the tumor microenvironment (TME). The programmable CQDs with chemotherapeutic drugs and immune enhancers (*e.g.*, Fe^{3+} ions, anti-PD1, and anti-PD L1) could enhance the antitumor property without any adverse effects *in vivo.*[24] CQDs modified with hydrazone bonds enhanced Dox release at an acidic pH (pH 5.5).[27] In another study, a hydrophobic cysteine-based polymer was conjugated with black phosphorus carbon dots (PCQDs) for the selective delivery of drugs in tumor cells.[28] Several CQD-based DDVs for targeted drug delivery have been described previously; however, the use of polyphenolic CQDs as DDVs has not been well reported.

Based on this understanding, we developed a polyphenolic green emissive TP excitable CQDs (*g*-CQDs) for selective cell membrane targeting and nuclear-specific drug delivery for synergistic tumor therapy (Scheme 1). The *g*-CQDs were prepared from phloroglucinol (a triangulogen) *via* a dehydration-induced ring fusion mechanism in a concentrated sulfuric acid medium by a wet chemistry-based thermal heating process. The developed *g*-CQDs showed a characteristic emission at 516 and 470 nm following OP and TP excitation at 350 and 800 nm. Dox was conjugated with *g*-CQDs (DLE 54.62%) *via* electrostatic interactions and exhibited a controlled release in acidic pH environment (5.0–6.5), which resembles the intracellular pH of tumor cells. The polyphenolic *g*-CQDs exhibit a quantum yield of 21.4% with superior one- and two-photon bioimaging properties with selective targeting at the cell membrane. The novelty of this work is to design an innovative cell-membrane targeting and nuclear drug delivery probe that have both real-time tracking and theranostic property for synergistic tumor therapy.

2. Results and discussion

2.1. Formation mechanism of *g*-CQDs

The *g*-CQDs were prepared *via* a thermal heating process using the three-fold symmetric polyphenolic compound, phloroglucinol (benzenetriol; C_{3h}; symmetry elements: E, C_3, C_3^2, σ_h, S_3, and S_3^{-1}).[18,29] Polyphenolic compounds tend to form carbonaceous structures through dehydration-induced ring fusion in a sulfuric acid (H_2SO_4) medium.[29] The presence of electron-

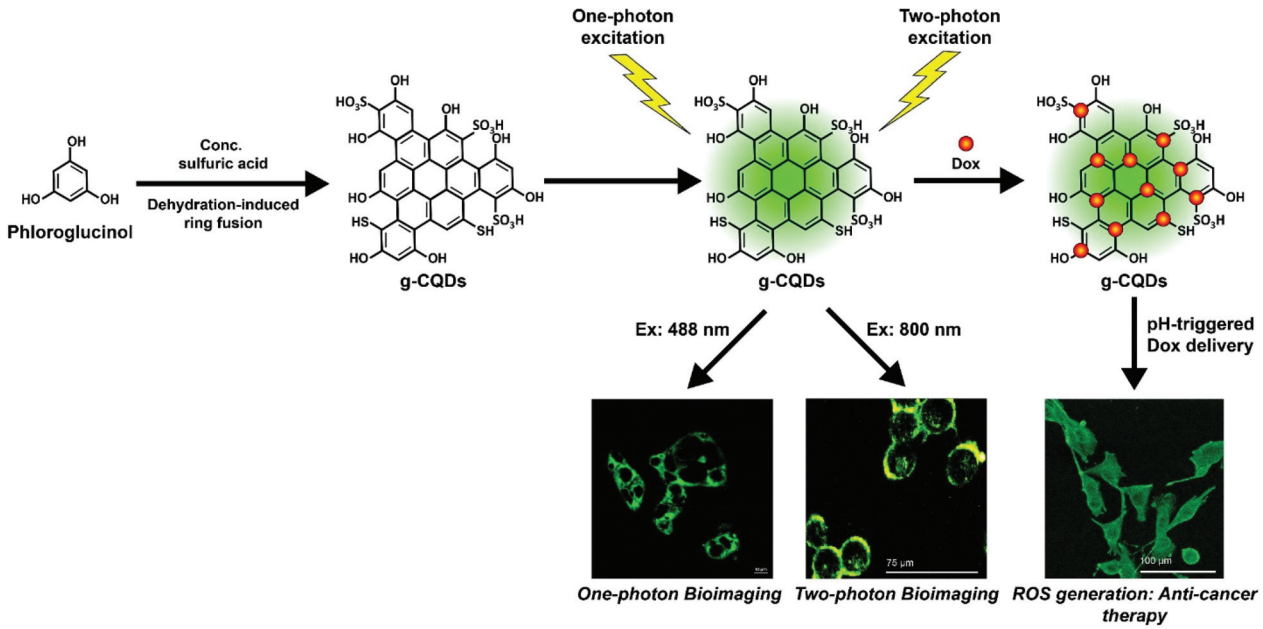

Scheme 1 Schematic illustration of the *g*-CQD-based nano-delivery system with real-time membrane tracking ability for tumor therapy.

donating hydroxyl groups (–OH) in phloroglucinol makes it highly reactive because of the three reactive protons [H^+] that are present at *meta*-position to each other.[17,29] In this study, polyphenolic *g*-CQDs were synthesized by a facile thermal heating process for 56 min. During the thermal reaction (190 °C), several phloroglucinol molecules underwent dehydration-induced ring fusion to produce *g*-CQDs by eliminating active –H and –OH groups. The digital photograph of the purified *g*-CQDs is shown in Fig. S1.† The mechanism for *g*-CQD formation was evaluated using ^{1}H-NMR and ^{13}C-NMR, and the results are shown in Fig. 1. The ^{1}H-NMR spectra of *g*-CQDs showed several resonance signals compared to the precursor within δ = 7.4–7.6 ppm, which correspond to the polyaromatic protons of *g*-CQDs, suggesting that many phloroglucinol molecules fused to form a sizeable polyaromatic structure (Fig. 1a). Moreover, various resonance signals at δ = 6.5–6.9 ppm also indicate several active protons of the –OH and –SH/–SO_3H groups of the *g*-CQDs. To gain an insight into the structural features, we investigated the ^{13}C-NMR spectra (Fig. 1b). The *g*-CQD spectra exhibited several resonance signals compared to the precursor at δ = 145–166 ppm, indicating the presence of sp^2 conjugated carbon atoms connected to the neighboring –OH groups at the edges. Interestingly, the resonance signals around 115–140 ppm indicate the formation of a large sp^2 polyaromatic core of the *g*-CQDs. The ζ-potentials of phloroglucinol and the *g*-CQDs were calculated to be −32.4 and −63.8 mV, respectively (Fig. S2†). The higher electronegativity of the *g*-CQDs further demonstrated the polyaromatic nature and the larger size of the formed *g*-CQDs with more hydroxyl groups, compared to the precursor molecule.

2.2. Morphological, functional, and optical properties of *g*-CQDs

To investigate the structure and morphology of the *g*-CQDs, high-resolution transmission electron microscopy (HR-TEM), X-ray diffraction (XRD), and Raman spectroscopy were utilized.

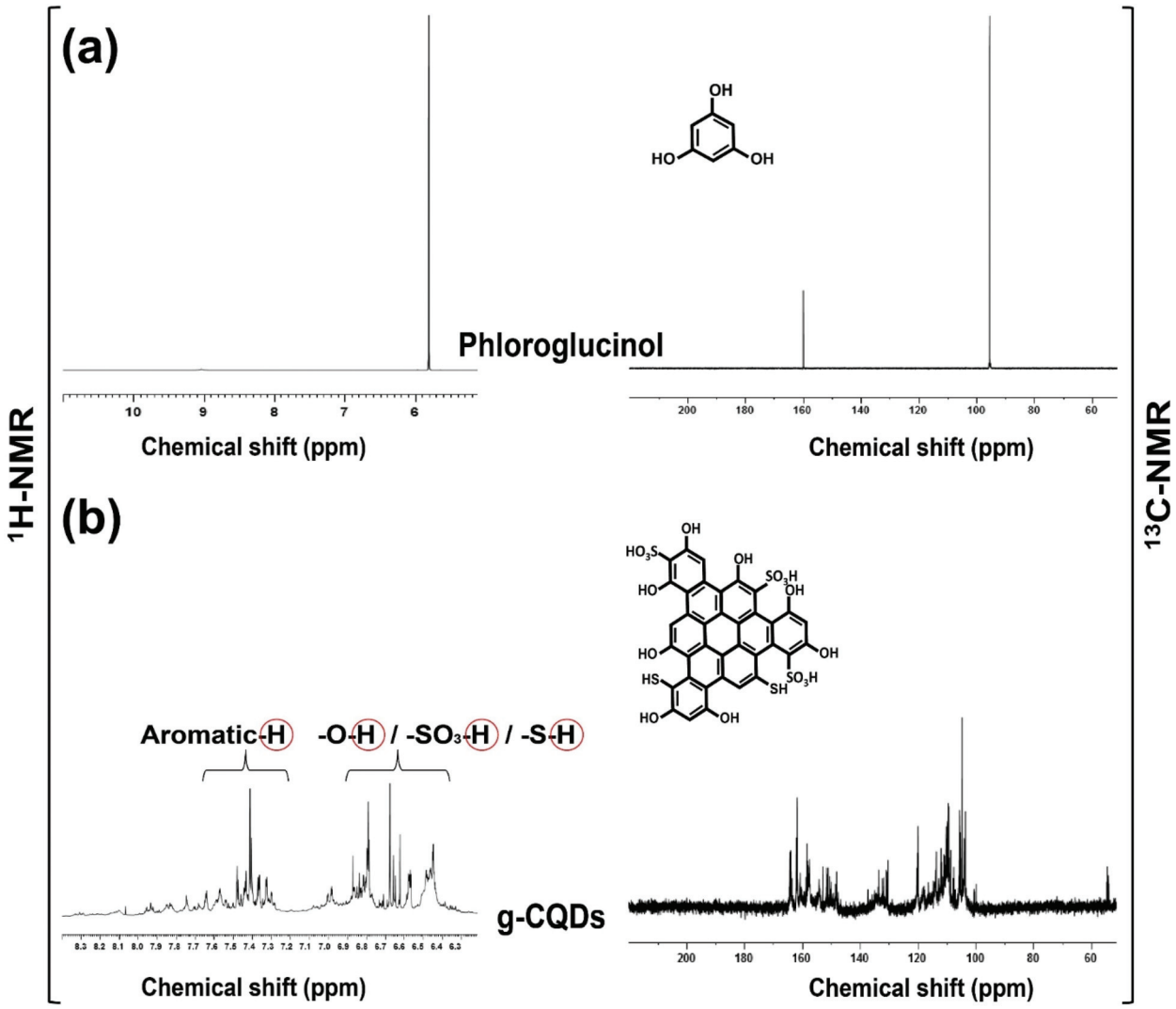

Fig. 1 (a) ^{1}H-NMR and (b) ^{13}C-NMR spectra of phloroglucinol and *g*-CQDs.

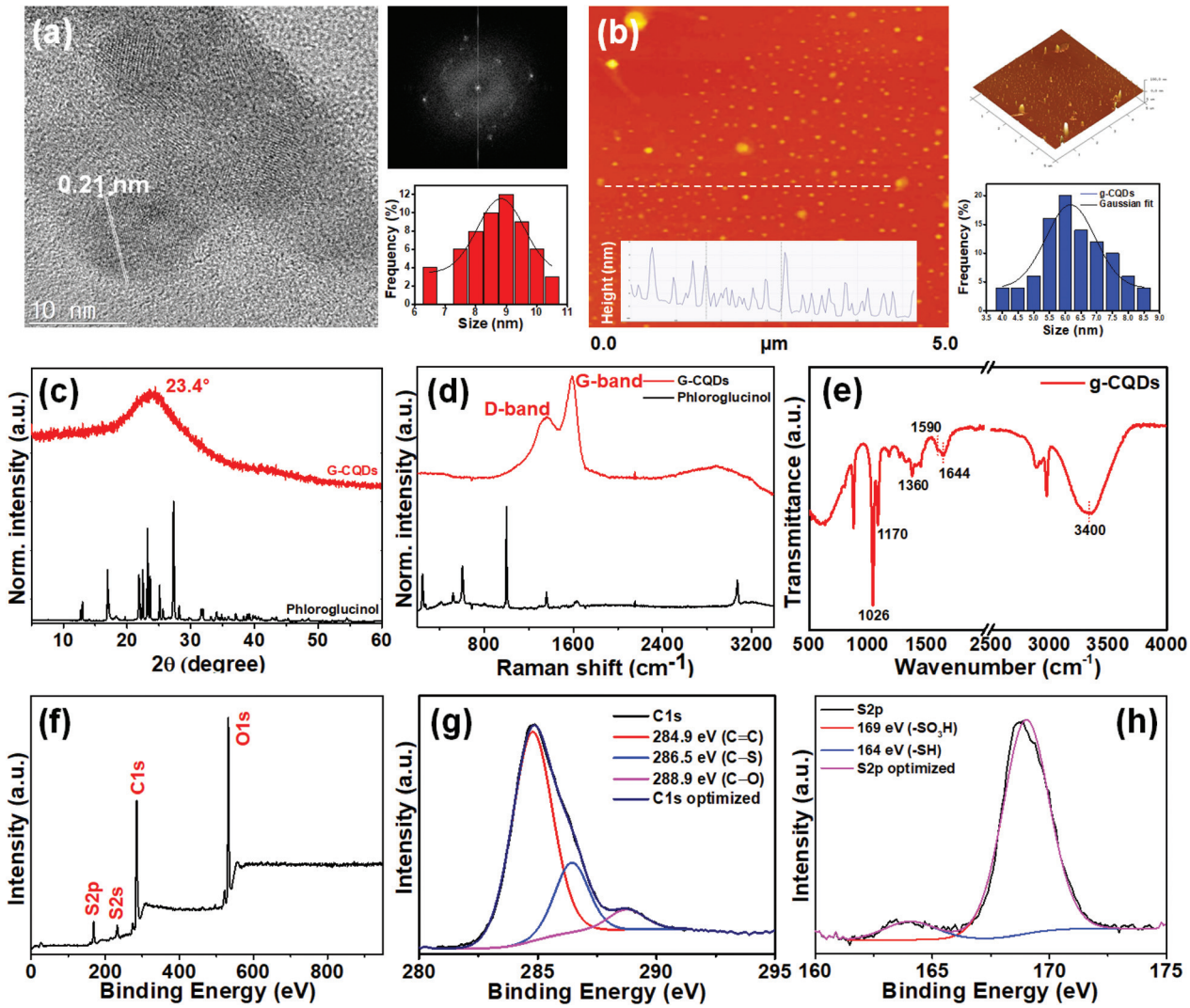

Fig. 2 (a) HR-TEM image with corresponding fast Fourier transform (FFT) pattern and size distribution of *g*-CQDs. (b) AFM image with corresponding height profile, 3D height topology image, and size distribution of *g*-CQDs. Scale bar: (a) 10 nm and (b) 5 μm. (c) XRD pattern, (d) Raman spectra, (e) FT-IR spectra of phloroglucinol and *g*-CQDs. (f) XPS total survey spectra of *g*-CQDs. (g) High-resolution C 1s, and (h) S 2p XPS spectra of *g*-CQDs.

The HR-TEM morphology of the *g*-CQDs showed a distinctive crystalline structure with a size distribution of 4–8 nm (Fig. 2a). Interestingly, the crystal lattice spacing for *g*-CQDs was 0.21 nm, indicating the inter-planar distance of the (100) plane, which revealed the defect-free graphene structure.[29] Moreover, the fast Fourier transform (FFT) pattern of *g*-CQDs revealed two distinct crystal plains, elucidating that they consist of one or two graphene layered structures, which was supported by the AFM images (Fig. 2b).[30,31] The lateral size distribution of the *g*-CQDs was about 6.2 ± 0.49 nm, respectively, which is consistent with the TEM results. The XRD patterns of phloroglucinol and the *g*-CQDs are given in Fig. 2(c). Notably, phloroglucinol exhibited a highly crystalline structure and showed a characteristic peak at θ = 16.8°, 21.6°, 22.9°, 25.4°, and 27.3°. However, these peaks disappeared entirely and formed a broad peak representing the (001) facet of the graphene structure at θ = 23.4°. The gradual broadening of the XRD peak from phloroglucinol to *g*-CQDs is due to the dehydration-mediated ring fusion and graphitization.[29,32] The intrinsic structure of the *g*-CQDs was investigated by Raman spectroscopy, and the results are shown in Fig. 2(d). Interestingly, the *g*-CQDs exhibited two characteristic peaks at approximately 1340 and 1590 cm^{-1}, corresponding to the graphitic structure's D-band and G-band, respectively. The D-band and G-band of the prepared *g*-CQDs indicated the presence of defects or disordered carbon due to surface oxidation and the sp^2 hybridized carbon framework, respectively.[17,18] Moreover, the (I_G/I_D) ratio of more than unity further demonstrates the formation of high-quality crystalline graphene nanostructures, which is supported by the HR-TEM and XRD results.

Next, the surface functional groups and chemical composition of the *g*-CQDs were investigated by Fourier-transform

infrared (FT-IR) and X-ray photoelectron spectroscopy (XPS). As shown in Fig. 2(e), the FT-IR spectra of *g*-CQDs showed typical stretching vibration peaks at 1170 and 3400 cm^{-1}, which correspond to the C–O/C–S and O–H groups, respectively. The peak around 1590 and 1644 cm^{-1} was observed due to the C=C stretching vibration, which signifies the presence of polyaromatic CQDs.[33,34] Moreover, the stretching vibrations at 1360 and 1026 cm^{-1} were ascribed to the sulfonyl group ($-SO_3H$), which indicates the presence of –OH and $-SO_3H$ groups on the surface of *g*-CQDs.[35] The XPS survey spectra showed the presence of three different elements (S, C, and O) in the *g*-CQDs (Fig. 2f). To investigate the elemental state, high-resolution C 1s XPS spectra were obtained, which confirmed the presence of three peaks at 284.9 eV, 286.2 eV, and 288.9 eV, corresponding to C=C, C–S, and C–O, respectively (Fig. 2g).[36] The S 2p spectra of *g*-CQDs also exhibited two peaks at 164 eV and 169 eV, which implies the presence of –SH and $-SO_3H$ (Fig. 2h).[9,37,38] This was due to the oxidation and sulfonation of phloroglucinol molecule at high temperature during g-CQDs synthesis which favoured the formation of large polyaromatic CQDs with C=C, C–S, C–O, O–H, –SH, and $-SO_3H$ groups. Therefore, diversity in the surface functional groups and the unique crystalline structure of *g*-CQDs play the principal role in demonstrating the optical properties associated with the quantum confinement effect.[39]

The optical properties of the *g*-CQDs were investigated by ultraviolet-visible (UV-Vis) and photoluminescence (PL) spectroscopy. Likewise, the *g*-CQDs showed excellent dispersibility in ethanol and ethanol–water. The ethanol-dispersed *g*-CQDs showed a characteristic peak at 288 nm, indicating the $\pi \rightarrow \pi^*$ transition of polyaromatic –polyphenolic rings (Fig. 3a). The PL spectra also showed an emission peak at approximately 516 nm, corresponding to green emission. The excitation-dependent PL emission spectra were also recorded, showing a minor excitation-dependent emission with maximum emission (λ_{em}) at 350 nm (Fig. 3b). Moreover, NIR responsive upconversion PL behavior was investigated. G-CQDs exhibited upconversion fluorescence emission at the wavelength around 470 nm (Fig. 3c). The QY of the *g*-CQDs was recorded using quinine sulfate (QY: 54% in 0.1 M H_2SO_4) as a reference value. The

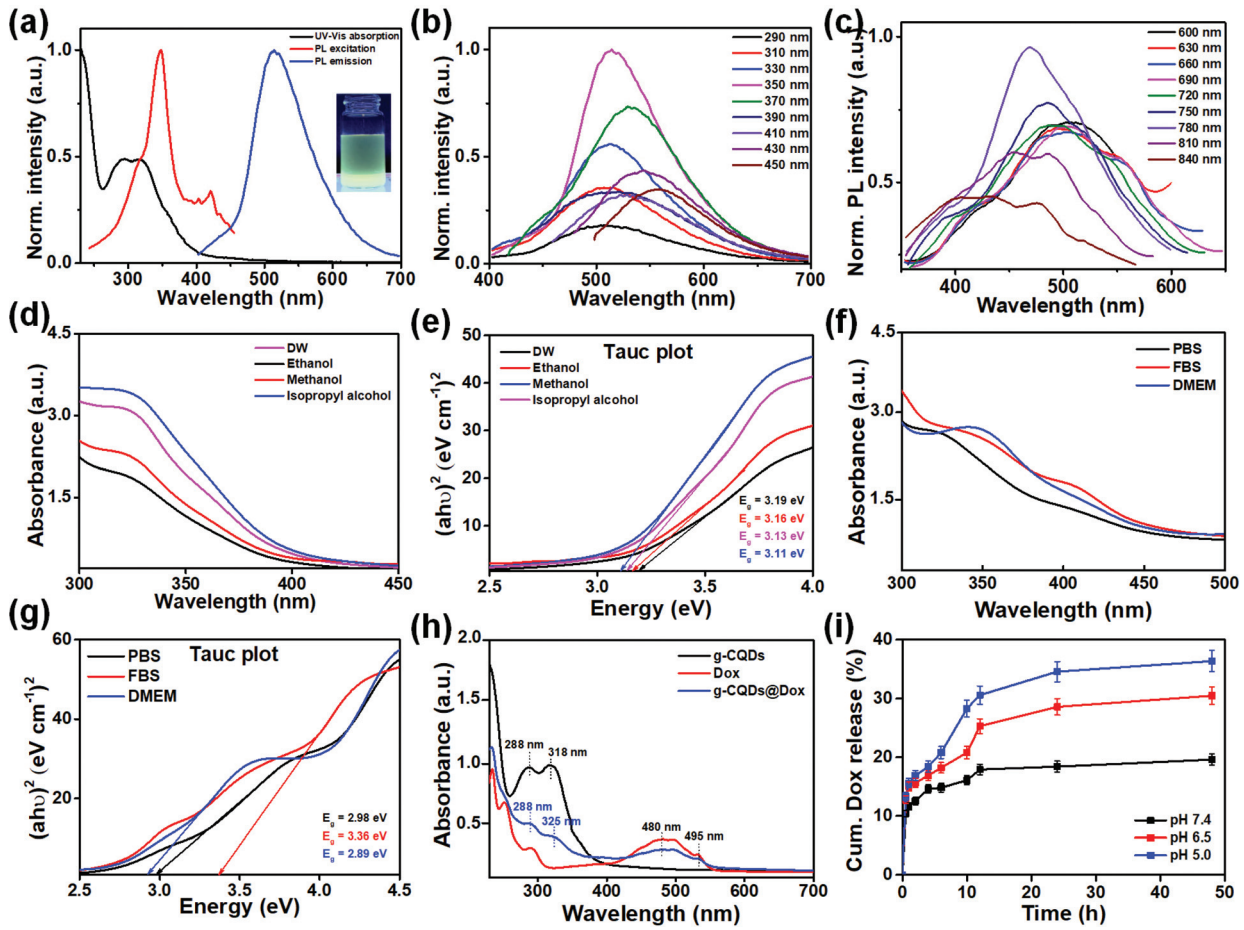

Fig. 3 (a) UV-Vis and PL excitation (red line)/emission (blue line) spectra of *g*-CQDs. (b) One-photon (OP) and (c) Two-photon (TP) fluorescence emission spectra of *g*-CQDs. (d) UV-Vis spectra of the as-prepared *g*-CQDs in water (DW), ethanol, methanol, and isopropyl alcohol (IPA) and (e) corresponding band gap energies. (f) UV-Vis spectra of the as-prepared *g*-CQDs in various biological fluids (PBS, FBS, and DMEM) with (g) corresponding band gap energies. (h) UV-Vis spectra of *g*-CQDs, free Dox, and *g*-CQDs@Dox complex. (i) Drug release kinetics of *g*-CQDs@Dox complex at pH 7.4, pH 6.5, and pH 5.0.

Table 1 Comparison of the various CQDs conjugated with Dox from the literature

Materials	Synthesis procedure	Dox loading efficiency (%)	Tumor cell	Ref.
Citric acid and ethylenediamine	Hydrothermal	57.5%	L929	40
Milk	Hydrothermal	87%	L929	20
4-Hydrazinobenzoic acid	Thermal	52.8%	A549	22
Citric acid and Boronic acid	Hydrothermal	84.28%	HeLa	9
Polyethyleneimine and glycerol	Hydrothermal	35.88%	MHCC-97L and Hep3B	8
4-Aminophenol and KIO_4	Solvothermal	21%	HeLa	41
Citric acid and hyaluronic acid	Hydrothermal	18.13%	4T1	42
Melanin	Ultrasonication	21.0%	4T1	24
Citric acid, ammonia, and Pt(IV)	Hydrothermal	28.0%	MGC-803	43
Folic acid	Pyrolysis	3.2–4.4%	MDA-MB-231	44
Carbon powder	Acid reflux	34.2–70%	SJ-GBM2	27
Phloroglucinol	Thermal heating	54.62%	B16F10 and MDA-MB-231	Present work

absolute QY of the *g*-CQDs was determined to be 21.4% (Fig. S3†). The lower QY was probably due to the high surface oxidation of *g*-CQDs in sulfuric acid medium.[29,39] A comparison table for the synthesis procedure and application of various CQDs with drug delivery efficiency from the literature is shown in Table 1.

2.3. Solvatochromic effect of *g*-CQDs

Solvatochromic behavior is a crucial technique for determining the fluorescence properties of CQDs for biological applications, particularly for bioimaging.[45,46] For this, we evaluated the stability of the *g*-CQDs in various solvents (water, ethanol, methanol, and isopropyl alcohol) and biological fluids (PBS, FBS, and DMEM) for 7 days (Fig. S4†). Then, the stability of the *g*-CQDs was monitored using a spectrophotometer. As shown in Fig. 3(d), the *g*-CQDs exhibited no observable change in the absorbance spectra, followed by bright fluorescence in all solvents. The bandgap energies of *g*-CQDs dispersed in DW, ethanol, methanol, and isopropyl alcohol were calculated as 3.19 eV (73.56 kcal mol^{-1}), 3.16 eV (72.86 kcal mol^{-1}), 3.13 eV (72.11 kcal mol^{-1}), and 3.11 eV (71.71 kcal mol^{-1}), respectively (Fig. 3e). A similar pattern of the UV-Vis spectrum was observed when the *g*-CQDs were incubated with biological fluids. As shown in Fig. 3(f), a slight bathochromic shift of the spectra was observed from PBS → DMEM, which was probably due to the decreased bandgap energies (2.98 eV → 2.89 eV) (Fig. 3g). Since biological fluids contain various metal ions,[47] we further investigated the effect of various metal ions (Zn^{2+}, Ag^{2+}, Ca^{2+}, Cu^{2+}, Mg^{2+}, and Fe^{3+}) on the stability of *g*-CQDs (Fig. S5†). Interestingly, there was no noticeable change in the absorbance spectra (A/A_0) for *g*-CQDs (0.15 mg mL^{-1}) after the addition of metal ions (100 μM), with an exception for Fe^{3+}, where a slight decrease was observed. These results demonstrate that the *g*-CQDs are feasible with biological fluids, which is highly favorable for bioimaging applications.[46,48]

2.4. Characterization of *g*-CQDs@Dox complex

Based on the superior optical and functional properties of *g*-CQDs, we investigated the binding efficiency of Dox with *g*-CQDs *via* UV-Vis spectroscopy, PL, FT-IR, and zeta potential measurements. As shown in Fig. 3(h), the *g*-CQDs exhibited absorption at 288 and 318 nm. Two absorption peaks for free Dox at 480 and 495 nm were also clearly observed. However, a slight change in the peak intensity (318 → 325 nm) for *g*-CQDs was observed in the presence of Dox, which was possibly due to the quenching of the *g*-CQD absorption spectra. The bathochromic shift (red shift) of CQDs in the presence of Dox has been reported previously as proof for the successful binding of Dox with CQDs.[22,40] The shifting of absorption peaks in *g*-CQDs@Dox compared to pure *g*-CQDs can also be explained by the strong π–π interaction between Dox and *g*-CQDs and indicated in the fluorescence resonance energy transfer (FRET) process from *g*-CQDs to Dox.[21,49] Moreover, the Tauc plot demonstrated a decrease in band gap from *g*-CQDs (E_g = 4.36 eV, 100.54 kcal mol^{-1}) to *g*-CQDs@Dox (E_g = 3.81 eV, 87.85 kcal mol^{-1}), which further indicated the interaction between Dox and *g*-CQDs (Fig. S6a†). The decreased bandgap was due to the FRET mechanism from *g*-CQDs to Dox, as shown in Fig. S6(b).† Moreover, the PL emission spectra for *g*-CQDs@Dox clearly indicate a shifting of emission spectra after incorporation of Dox (Fig. S7a†). After the formation of π–π stacking interaction between Dox and *g*-CQDs, the π–π stacking system showed hypsochromic shift in the emission peak as shown in the digital images as well as emission spectra (Fig. S7b†). The FT-IR spectra for pure *g*-CQDs, free Dox, and *g*-CQDs@Dox are shown in Fig. S8.† In *g*-CQDs, the absorption band at 3351 cm^{-1} corresponds to the O–H (hydroxyl) stretching vibrations. The peaks at 2975 cm^{-1}, 1645 cm^{-1}, and 1590 cm^{-1} are assigned to the C–H (alkene sp^2), C═O (carbonyl), and C═C stretching vibrations of polyphenolic CQDs.[33,50] Moreover, absorption peaks between 1368 cm^{-1} and 1044 cm^{-1} were observed, indicating $-SO_3H$ (sulfonyl) moieties in the *g*-CQDs. In the FT-IR spectra of Dox, we observed peaks around 1637 and 3308 cm^{-1} corresponding to the C═O and O–H stretching vibrations, respectively. Interestingly, the *g*-CQDs@Dox system resembles the spectra of DOX with a slight variation and the chemical functional groups of CQDs are less prominent probably due to the very high intensity of the C═O and O–H stretching vibrations peaks of Dox. Moreover, the zeta potential (ζ) of the *g*-CQDs and *g*-CQDs@Dox was also recorded to confirm the formation

of strong electrostatic interaction. As shown in Fig. S9,† the ζ-potentials of *g*-CQDs, free Dox, and *g*-CQDs@Dox were −34 mV, 14 mV, and −21.8 mV, respectively. The decreased electronegativity of *g*-CQDs@Dox explains the successful binding of Dox with *g*-CQDs.[9,40,49–51]

2.5. Dox-loading and pH-responsive release efficiency

The *g*-CQDs were loaded with a standard anti-cancer drug, Dox, *via* electrostatic interactions. Briefly, 1 mL of Dox (500 μg mL^{-1}) was added to 1 mL of *g*-CQDs (5 mg mL^{-1}) at pH 7.4 for 24 h. The resulting solution was purified and dried at 60 °C to obtain a powder. Tumor cells exhibit an acidic pH microenvironment,[20,52,53] and an ideal nanocarrier with a pH-responsive delivery property is crucial for targeting the tumor cells.[54,55] The dispersion property of the *g*-CQDs (5 mg mL^{-1}) at varying pH (5.0, 6.5, and 7.4) was photographed, and the results are shown in Fig. S10.† Interestingly, the pH alteration did not alter the fluorescence property of the *g*-CQDs even at pH 5.0, indicating that there was no structural change in the *g*-CQDs. The Dox loading efficiency (DLE) and loading content (DLC) were analyzed by measuring the absorbance at 485 nm, and the amounts were calculated as 54.62% and 323.25 μg mL^{-1}, respectively. These results are consistent with previous reports and demonstrate that our *g*-CQDs had excellent loading efficiency for Dox.[20,54] The possible mechanism of Dox loading involves the electrostatic interaction of Dox with *g*-CQDs. As demonstrated earlier, the *g*-CQDs (ζ = −34 mV) have several electronegative groups (–OH and $–SO_3H$) on the surface; therefore, the Dox molecule interacted with *g*-CQDs through stable hydrogen bond formation,[56] and this phenomenon was also explained by the reduced ζ-potential (−21.8 mV) of the *g*-CQDs@Dox complex. Moreover, the π–π stacking interaction also favors the DOX loading effectively as discussed earlier.

For the pH-responsive drug release test, 10 mL of the *g*-CQDs@Dox complex was taken in various pH buffers (pH 5.0–7.4) and placed on a shaker at 150 rpm at 37 °C. The % Dox release was calculated by recording the absorbance at 485 nm, and the results are shown in Fig. 3(i). Notably, a higher quantity of drug release was observed at both pH 5.0 and 6.5, than at pH 7.4, indicating the selective release of Dox. The intracellular pH of tumor cells is moderately acidic ranging from 6.2 to 6.9, compared to healthy cells.[57,58] Therefore, a promising drug delivery strategy based on selective delivery is highly favorable for the targeted delivery of chemotherapeutic drugs.[59,60] In our study, the controlled release of Dox from *g*-CQDs signifies its potential application as a nanotheranostic probe for cancer therapy. Interestingly, the Dox release profile at pH 5.0 and 6.5, further suggests that the developed probe is suitable for a long time for site-specific delivery of chemotherapeutic drugs to tumor cells during intracellular pH fluctuation.[61] Taken together, the *g*-CQDs@Dox complex demonstrated a highly pH-responsive and smart release of Dox molecules, which could be used as an ideal drug carrier for various chemotherapeutic drugs for anticancer therapy.

2.6. *In vitro* anti-tumor efficacy and ROS mechanism

The *in vitro* cytotoxicity of B16F10 cells in the presence of *g*-CQDs was evaluated using the WST-8 assay. As shown in Fig. S11(a),† the viability of tumor cells gradually decreased as the concentration of *g*-CQDs increased from 0.01 to 0.15 mg mL^{-1} after 24 h of incubation. At a low concentration (0.01 mg mL^{-1}), there was no apparent change in the viability of B16F10 cells (~98% as of control). However, at a higher concentration (0.15 mg mL^{-1}), the viability of B16F10 cells significantly decreased (~80% as of control). Therefore, it can be concluded that the *g*-CQDs alone had moderate cytotoxicity on B16F10 cells at 0.15 mg mL^{-1} concentration. To support this finding, we performed a time-dependent viability test in the presence of *g*-CQDs. As shown in Fig. S12(b),† the *g*-CQDs (0.15 mg mL^{-1}) exhibited higher cytotoxicity (viability ~72% as of control) when incubated for up to 48 h, compared to the control groups, meaning that a combination therapy with *g*-CQDs@Dox would be effective to kill the tumor cells. Next, the cytotoxicity profile of Dox and *g*-CQDs@Dox was also investigated by the WST-8 assay in both B16F10 and MDA cells, and the results are shown in Fig. 4. Interestingly, the free Dox alone had serious cytotoxicity in both B16F10 (Fig. 4a) and MDA (Fig. 4b) cells; however, conjugation of Dox with *g*-CQDs (= *g*-CQDs@Dox) diminished the cytotoxicity of Dox, as shown in Fig. 4(c and d). Therefore, our results demonstrated that *g*-CQDs@Dox might have a controlled anti-tumor effect than free Dox. Although Dox exerted higher cytotoxicity on tumor cells, the *g*-CQDs@Dox complex is more suitable for killing tumor cells because of the controlled release of Dox and specific targeting of tumor cells.[20]

Based on the excellent cytotoxic nature of the *g*-CQDs@Dox complex, we evaluated the underlying mechanism of its *in vitro* anti-tumor properties. The antitumor mechanism was evaluated through 2′,7′-dichlorodihydrofluorecin diacetate (DCF-DA) staining, terminal deoxynucleotidyl transferase dUTP nick end (TUNEL) staining, and fluorescent activated cell sorting (FACS) analysis. As shown in Fig. 4e(i), the *g*-CQD-treated B16F10 cells produced considerable amounts of intracellular ROS after 24 h of incubation. Interestingly, the *g*-CQDs@Dox showed a significantly higher ROS accumulation than the *g*-CQDs and control groups, indicating that a combined therapy of the *g*-CQDs@Dox system is sufficient to elevate ROS in tumor cells. This was further explained by FACS analysis of B16F10 cells, as shown in Fig. 4e(ii). The strong green fluorescence in the cytoplasm is due to the higher accumulation and higher affinity of *g*-CQDs@Dox towards cell organelles in tumor cells.[20,62] Since Dox is known to target DNA and induce DNA damage,[59] we investigated the DNA damage mechanism *via* TUNEL assay, and the results are shown in Fig. 4e(iii). Notably, intrinsic damage to DNA was observed in both *g*-CQD and *g*-CQDs@Dox treated cells. However, following *g*-CQDs@Dox treatment, the BrdU FL intensity was significantly enhanced, and the propidium iodide (PI) FL intensity decreased, demonstrating that the designed probe traveled inside the nucleus and amplified the

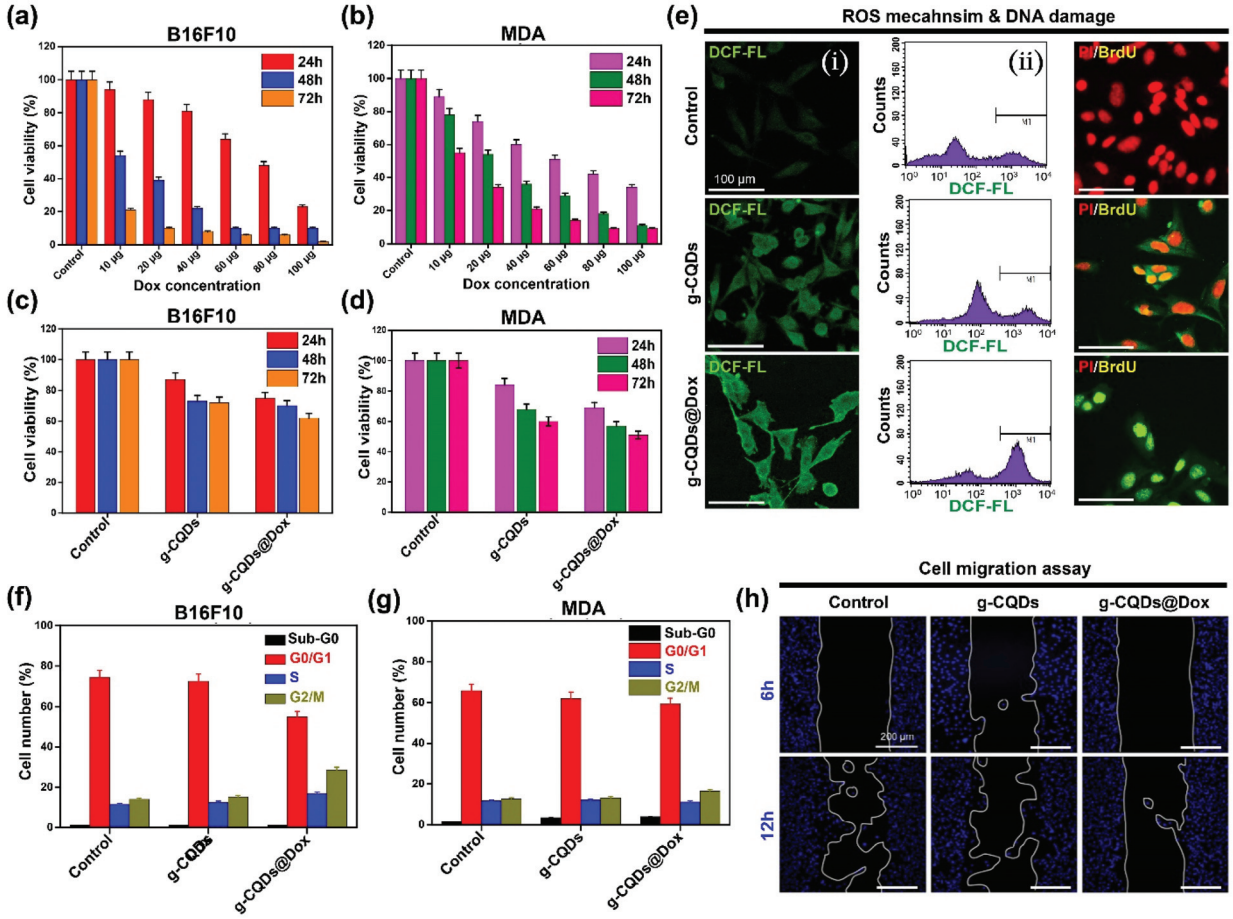

Fig. 4 *In vitro* antitumor efficacy of *g*-CQDs and *g*-CQDs@Dox complex. (a and b) B16F10 and MDA cell viabilities after incubation with different Dox concentrations for 72 h. (c and d) B16F10 and MDA cell viabilities after incubation with *g*-CQDs and *g*-CQDs@Dox at indicated time intervals. (e) Evaluation of ROS and DNA damage mechanism in B16F10 cells. Representative DCF-DA staining (i), FACS (ii), and BrdU staining (iii) against B16F10 cells after 48 h of incubation with *g*-CQDs and *g*-CQDs@Dox, respectively. (f & g) Cell cycle distribution analysis of B16F10 and HepG2 cells after 48 h of incubation. (h) Cell migration assay following incubation with *g*-CQDs and *g*-CQDs@Dox against B16F10 cells. Data are mean ± s.d. (n = 3), statistical significance at $*p < 0.05$ (Student's t-test). Scale bar: (e) 100 μm and (h) 200 μm.

DNA damage. This phenomenon can be explained by the fact that CQDs tend to interact with DNA *via* π–π stacking and electrostatic interactions, leading to a base pair mismatch. The mismatched base pair and the unusual binding of CQDs often lead to cell cycle arrest and death of tumor cells.[63,64] Meanwhile, Dox was also found to interact with DNA by intercalating with specific base pairs (d[TATATA]$_2$), followed by the inhibition of DNA biosynthesis, interaction with topoisomerase II, cyclin-dependent kinase (CDK) inactivation, and DNA unwinding.[65] Our results demonstrated that the *g*-CQDs@Dox complex induces DNA damage and mitochondrial stress (intracellular ROS) by a 'dual mechanism' to kill the B16F10 cells.

Next, the cell cycle distribution analysis was performed to confirm the DNA damage mechanism. For this, the *g*-CQDs@Dox treated cells were stained with PI, and analyzed through FACS to study the DNA content in the cells. Notably, both the *g*-CQD and *g*-CQDs@Dox treated cells exhibited G2/M phase DNA damage in B16F10 (Fig. 4f) and MDA (Fig. 4g), which was consistent with the TUNEL assay. Besides, we also found a reduction in cell migration of tumor cells in the presence of *g*-CQDs@Dox compared to *g*-CQDs (Fig. 4h) after 12 h of incubation.

Since chemotherapeutic agents have a severe effect on cell morphology and dynamics,[66] we investigated the mechanism of cell damage and actin disruption. We studied F-actin dynamics and focal adhesion dynamics (Paxillin; focal adhesion protein) following *g*-CQDs@Dox treatment. B16F10 cells were incubated with *g*-CQDs and *g*-CQDs@Dox for 24 h and stained with an F-actin probe. The images were captured using a fluorescence microscope, and the average actin intensity was measured using the ImageJ software with Gaussian package tools. As shown in Fig. 5(a), the *g*-CQD-treated cells exhibited severe cytoskeletal stretching and fragmented actin particles, indicating that the *g*-CQDs could inhibit actin assembly proteins. Moreover, a gradual increase in actin intensity was observed when the cells were incubated with the *g*-CQDs@Dox complex compared to the control groups, indicating that the nanocarrier also had a potential effect on cytos-

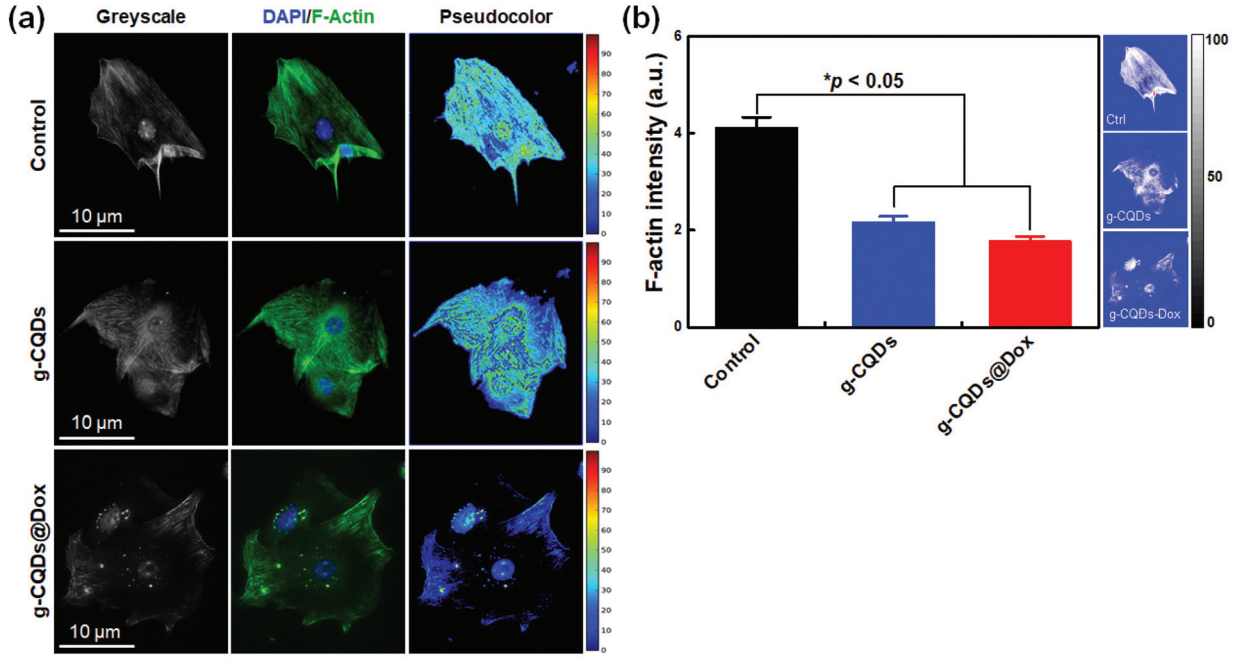

Fig. 5 F-actin distribution in B16F10 cells. (a) Representative fluorescence microscopy with corresponding pseudocolor merge images of B16F10 cells indicating the actin distribution. The cells were incubated with *g*-CQDs and *g*-CQDs@Dox for 24 h and stained with DAPI (nucleus) and F-actin probe (green). Scale bar: 10 μm. (b) Calculation of average actin intensity using the ImageJ Fiji software (OrientationJ and Gaussian package tool, NIH, Bethesda, USA). Asterisks indicate statistically significant differences between control and treated groups (*$p < 0.05$, Student's *t*-test), $n = 10$.

keleton disruption. The average actin intensities for the control, *g*-CQDs, and *g*-CQDs@Dox are shown in Fig. 5(b). To further emphasize cellular adhesion, we also studied Pax expression following nanocarrier treatment. As shown in Fig. S12(a),† the number of focal adhesion points decreased with *g*-CQD and *g*-CQDs@Dox treatment, which was explained by the reduced paxillin intensity from the tumor cells (Fig. S13b†). Taken together, our results demonstrate that the Dox-loaded *g*-CQD nanocarriers have a potential role in the regulation of cytoskeletal morphology during apoptotic cell death.

2.7. *In vitro* nuclear targeting and drug release properties

As direct evidence for intracellular drug delivery by the *g*-CQDs@Dox complex, we evaluated time-dependent Dox delivery in B16F10 cells. It was interesting to note that the *g*-CQDs were sufficiently localized inside the nucleus within 4 h of incubation, elucidating that *g*-CQDs have the potential to deliver several active molecules to the nucleus. Next, B16F10 cells were incubated with *g*-CQDs@Dox at 37 °C for 0.5, 2, and 4 h (Fig. 6). Free Dox was used for comparison. After the desired time point, the cells were stained with DAPI (blue, for nucleus), and the delivery efficiency was evaluated by checking the red and green fluorescence emitted from the Dox and *g*-CQDs. As shown in Fig. 6(a), the DAPI-stained cells exhibited bright blue fluorescence from the nucleus, leaving an opaque nuclear envelope, which was barely visible. After 0.5 h, Dox started to accumulate inside the nucleus, which was characterized by a clear nuclear envelope, indicating that Dox had successfully penetrated the nuclear pore. After 2 h and 4 h of incubation, the Dox fluorescence intensity increased (Fig. 6b and c), leaving a clear zone of accumulation.[9] The line-scan profile intensity for free Dox simultaneously increased from 0.5 h to 4 h of incubation, showing direct evidence of nuclear penetration of Dox. Meanwhile, the *g*-CQDs@Dox-treated cells exhibited both cytoplasmic and nuclear fluorescence, indicating that the *g*-CQDs acted as a carrier for Dox. Although the cytoplasmic fluorescence was slightly lower than the nuclear fluorescence, it can be stated that the *g*-CQDs@Dox complex traveled through the subcellular organelles and was transported to the nucleus. Notably, the Dox-loaded *g*-CQDs exhibited a decreased fluorescence signal after 4 h of incubation compared to free Dox (Fig. 6d–f). Therefore, it was concluded that the modification of *g*-CQDs with Dox lowered the delivery efficiency of Dox, but effectively entered the tumor cell nuclei, thus limiting the potential toxicity of Dox and controlling the delivery *via* pH alteration within the cell. Therefore, an eco-friendly approach for limiting the potential toxicity of chemotherapeutic drugs was successfully achieved through the *g*-CQDs@Dox complex, which could be used as an ideal candidate for drug loading and acidic-pH-driven drug release inside cell nuclei.[9,67]

2.8. One-photon and two-photon imaging of tumor cells

The *in vitro* bioimaging property of *g*-CQDs was evaluated in MDA cells through one- and two-photon cell imaging using a confocal laser scanning microscope. As shown in Fig. 7, the one-photon (OP) confocal images of MDA cells were obtained

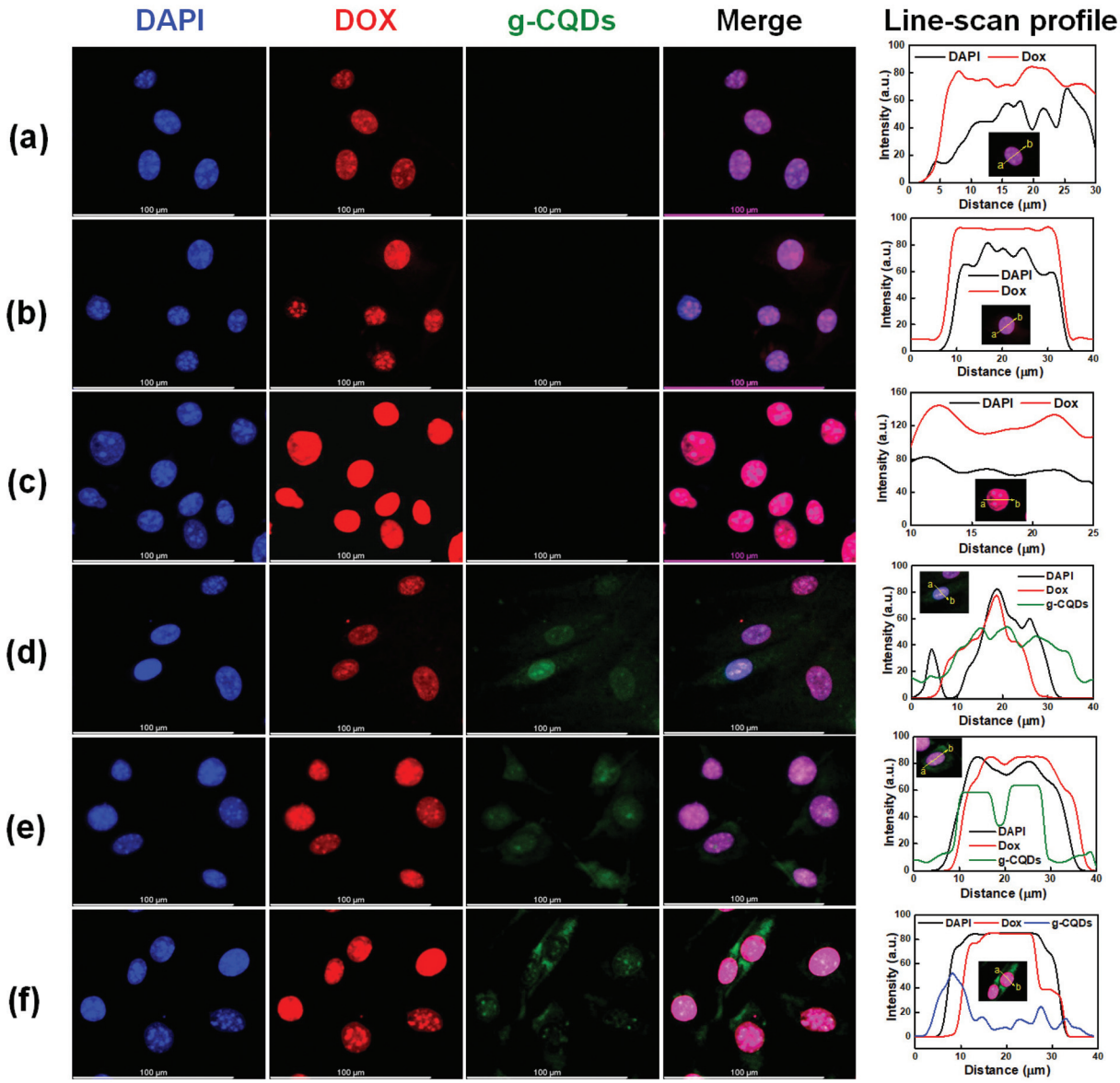

Fig. 6 Fluorescence images B16F10 cells showing free Dox uptake after (a) 0.5 h, (b) 2 h, and (c) 4 h, respectively. Fluorescence microscopy images of B16F10 cells loaded with *g*-CQDs@Dox after (d) 0.5 h, © 2 h, and (f) 4 h, with corresponding line-scan profile of the fluorescence intensity for DAPI (blue), Dox (red), and *g*-CQDs (green), respectively. Scale bar: 100 μm.

by incubating 10.0 μg mL^{-1} *g*-CQDs for 1 h. The concentration mentioned above was selected by monitoring concentration-dependent cell imaging experiments. In Fig. 7a, the *g*-CQDs were selectively localized at the membrane of the MDA cells after 1 h of incubation. The images at different laser excitations indicated that *g*-CQDs exhibited an extremely low fluorescence signal at 405 nm excitation; however, a bright green and yellow fluorescence was observed following 488 and 532 nm laser excitation. This was further supported by observing a pseudocolor merge image for all the channels, which showed that the *g*-CQDs only displayed ultra-bright fluorescence when excited with a 488 and 532 nm laser. The orthogonal projection *z*-stack images are shown in Fig. 7(b and c) in different excitation channels. To confirm the membrane targeting property of *g*-CQDs, we have performed a colocalization study against *g*-CQDs using a commercially available Colocalization dye (Dil). It is noteworthy that the fluorescence signals obtained from both the commercial dye and *g*-CQDs colocalized in the membrane with a Pearson coefficient of 0.597, and the percentage of colocalization was calculated as 18.14%, respectively (Fig. S13†). Indeed, the CQDs are extremely variable inside the cellular pH, and their behavior is quite heterogeneous with respect to cell lines; therefore, the one-photon imaging significantly varies with cell-to-cell heterogeneity and their exact localization.[68,69] Our results demonstrated that the as-prepared *g*-CQDs mainly targeted the cell

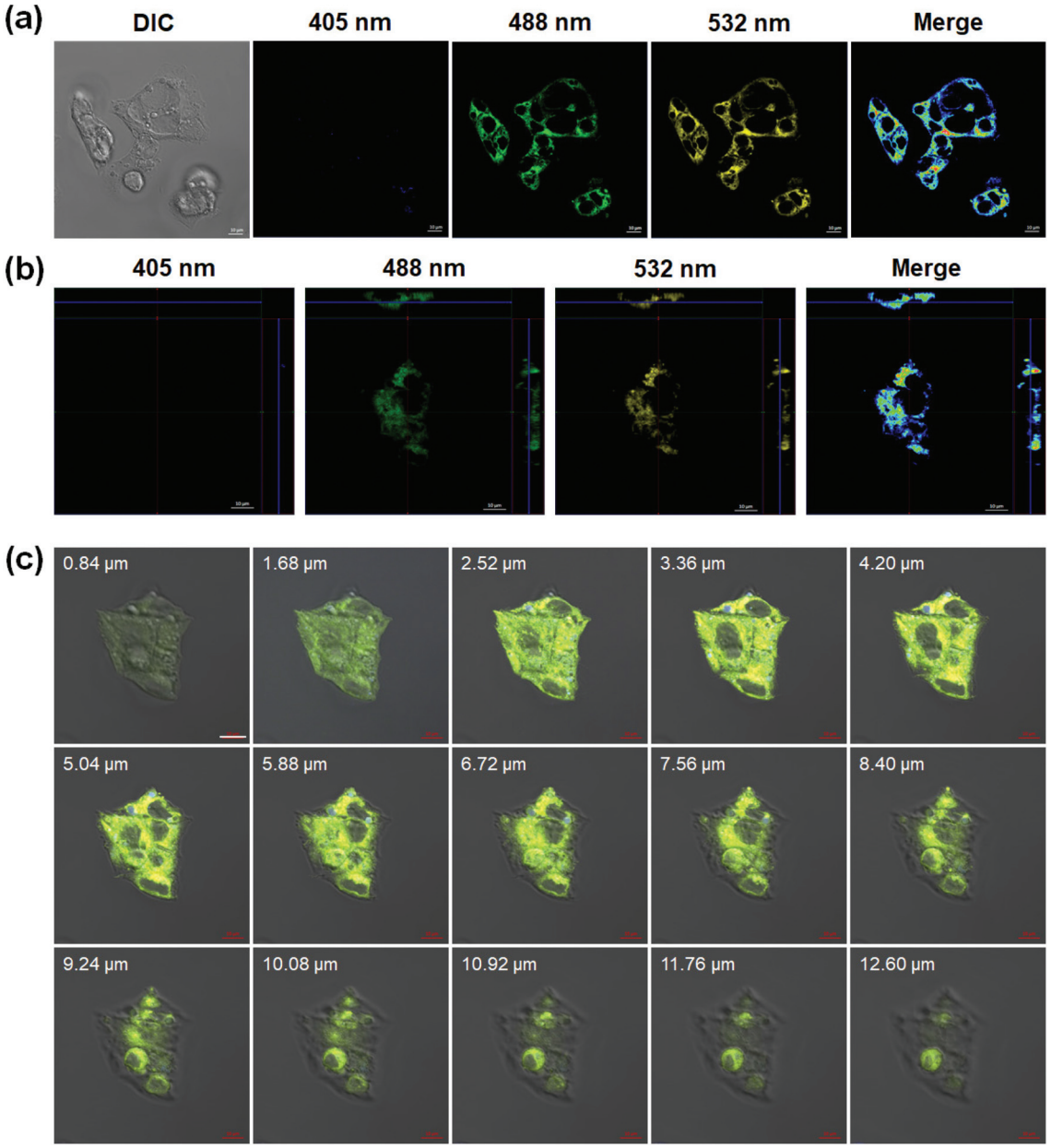

Fig. 7 (a) One-photon (OP) bioimaging of MDA cells under DIC, 405 nm (blue), 488 nm (green), 532 nm (yellow), and pseudocolor merge image following *g*-CQDs (10.0 μg mL^{-1}) treatment for 1 h. (b) Orthogonal projections of *z*-stack confocal images for MDA cells treated with *g*-CQDs. (c) Maximum intensity projection (MIP) *z*-stack images of MDA cells with 15 slices during OP bioimaging. The *z*-stack images were obtained starting in the middle of the cells in 0.84 μm intervals. Scale bar: 10 μm.

membrane and were slightly diffused in the cytoplasm. The two-photon (TP) cell imaging experiment was further performed to evaluate the membrane-targeting properties of *g*-CQDs, and the results are shown in Fig. 8. We selected the 800 nm TP excitation for cell imaging experiments since the emission intensity was higher at this wavelength. The TP excitation-dependent cellular intensity profile of MDA cells is shown in Fig. 8(a and b). As seen in the TP imaging, the *g*-CQDs are selectively localized in the membrane. Furthermore, the pseudocolor merge images showed that some part is staining the cytoplasmic region as we detected a faint signal from the cytoplasm (Fig. 8c). This was due to the slight diffusion of *g*-CQDs from the membrane to the cytoplasm. This phenomenon clearly indicated that the as-prepared *g*-CQDs principally localized in the cell membrane and have superior membrane-targeting properties for studying the roles of membrane-associated proteins in various physiological processes in tumor cells. Next, we investigated the photostability of *g*-CQDs for bioimaging applications. An exposure time of 60–600 s was applied to MDA cells during cell imaging at λ_{ex} =

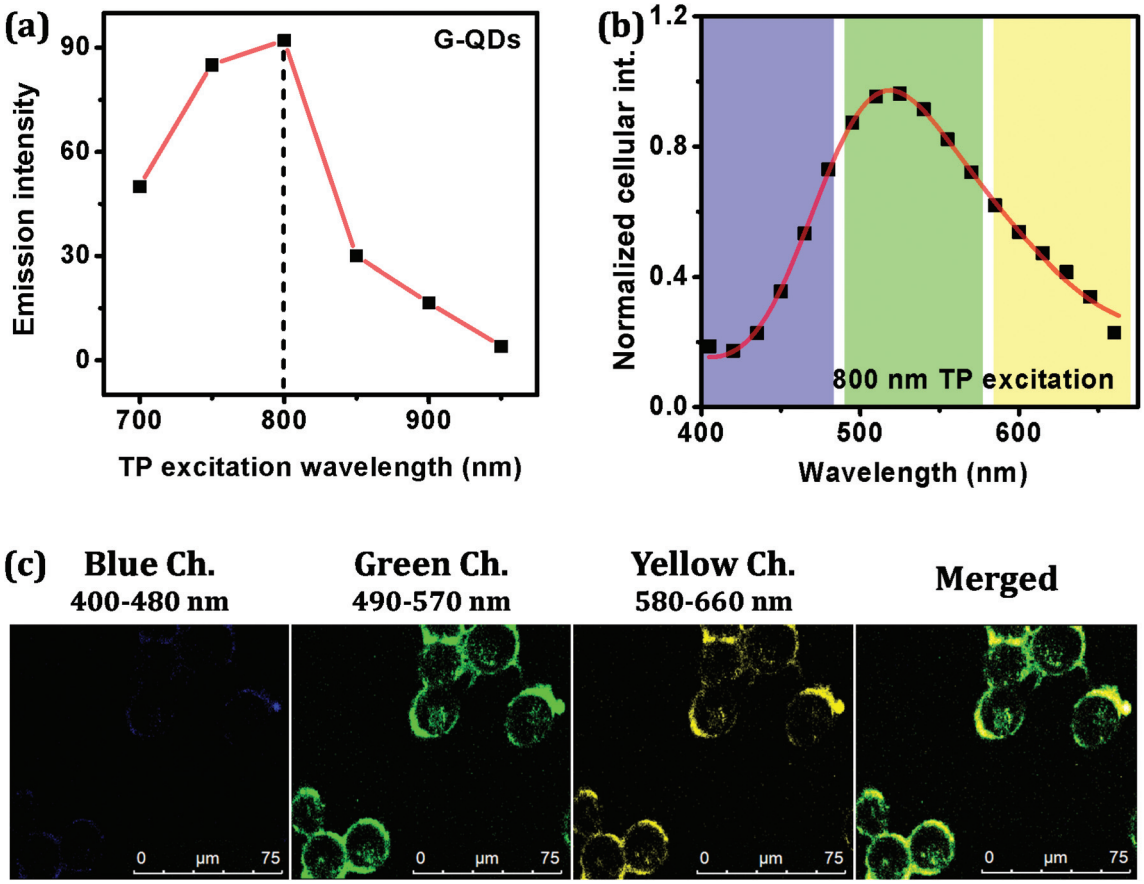

Fig. 8 (a) Two-photon (TP) excitation dependent cellular intensity profile for *g*-CQDs. Emission collection in 400–660 nm. (b) Cellular spectra of *g*-CQDs under 800 nm TP excitation. (c) Cellular images obtained under different collection channels. Blue: 400–480 nm, green: 490–570 nm; yellow: 580–660 nm. Intensity based pseudo color images are presented. MDA cells were treated with 10.0 μg mL^{-1} *g*-CQDs for 1 h, washed with pH 7.4 PBS two times and fixed with 4% formaldehyde prior to imaging.

488 nm, respectively. Strikingly, the MDA cells exhibited higher stability and less photobleaching even after 600 s of exposure to laser light (Fig. S14†). This phenomenon was due to the higher affinity of *g*-CQDs towards the membrane and membrane-associated proteins,[70–72] which was further evaluated by calculating the photobleaching percentage.

2.9. *In vivo* biocompatibility and biosafety analysis

One of the significant challenges in nanocarrier-based chemotherapy is the rapid elimination of the chemotherapeutic agents from the tumor sites, and therefore restricting the therapeutic efficiency of the agents. Likewise, an ideal nanotheranostic agent with an enhanced tumor penetration and retention (EPR) effect could serve as an effective treatment strategy for solid tumor therapy.[73] Before investigating the *in vivo* therapeutic efficiency, we checked the biocompatibility of the *g*-CQDs and *g*-CQDs@Dox *via* hemolysis tests. As shown in Fig. 9(a), *g*-CQDs and *g*-CQDs@Dox exhibited excellent blood biocompatibility compared to the control group. The RBCs were found to be healthy in both *g*-CQDs and *g*-CQDs@Dox treatment after 120 min of incubation, indicating their good cytocompatibility. Next, the pharmacokinetic profile of the *g*-CQDs@Dox was examined by fluorescence measurements to understand the biodistribution property in the blood and tumor sites after 72 h post-injection, respectively. As shown in Fig. 9(b), the *g*-CQDs@Dox showed the typical two compartment model of Dox penetration and retention. After the distribution phase (the first phase consisting of a single dose with a rapid decline) with a half-life ($t_{1/2}$) of 2.2 ± 0.3 h, the *g*-CQDs@Dox displayed a long elimination phase (the second phase of blood clearance) with $t_{1/2}$ of 24.2 ± 2.5 h. A similar kind of observation was recorded in tumor sites with a long retention period for *g*-CQDs@Dox ($t_{1/2}$ = 19.5 ± 0.5 h) (Fig. 9c). The relative volume of distribution (V) was calculated by measuring the area under curve (AUC) and is recorded as V_{blood} = 1.48 ± 0.9 mL and V_{tumor} = 3.16 ± 0.77 mL, respectively. Therefore, the long-term blood circulation and enhanced accumulation of *g*-CQDs@Dox in the tumor sites favored the macrophage clearance in the reticuloendothelial system (RES), showing an excellent EPR effect.[74] To confirm the EPR effect, we examined the tumor tissues *via* fluorescence staining after 6 and 12 h post-injection in tumor-bearing mice and the results are shown in Fig. 9(d). Notably, a higher accumulation of Dox (red fluorescence) was observed in the tumor samples

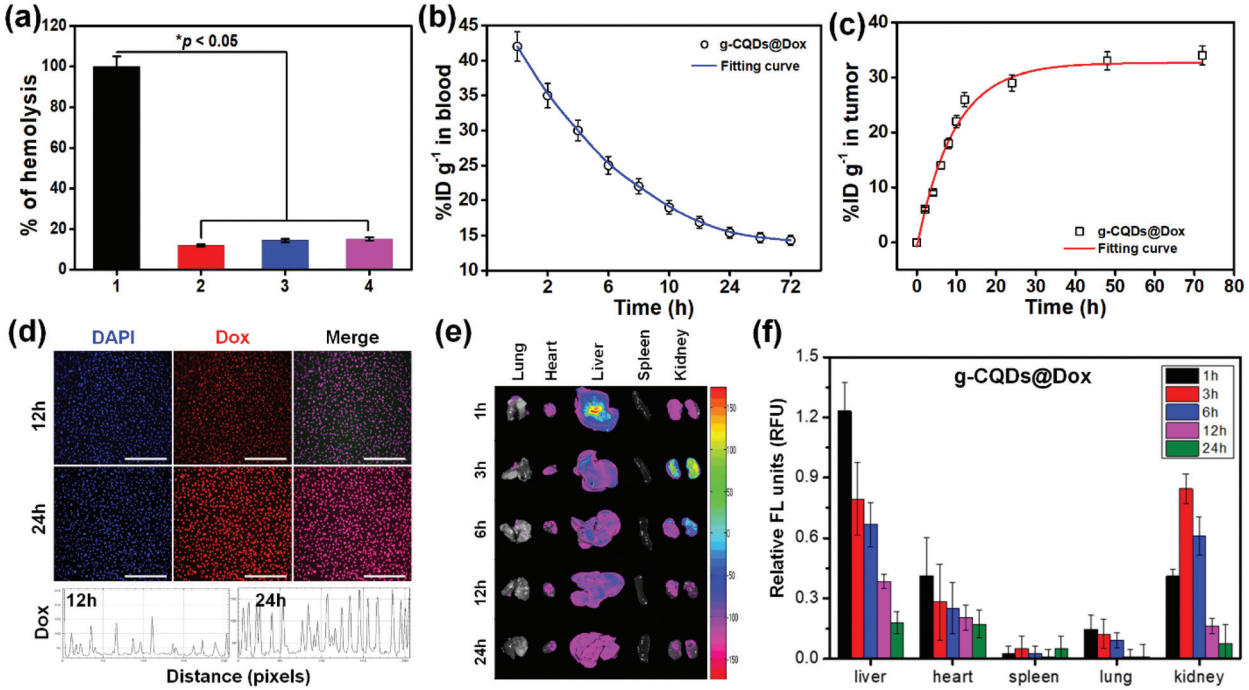

Fig. 9 *In vivo* cytocompatibility and pharmacokinetics. (a) Hemocompatibility test in the presence of *g*-CQDs and *g*-CQDs@Dox complex. (1) DW, (2) PBS, (3) Dox, and (4) *g*-CQDs@Dox. (b) The blood circulation curve of the *g*-CQDs@Dox as determined by the fluorescence intensities of *g*-CQDs in B16F10 tumor-bearing mice at indicated time intervals. (c) The relative amount of *g*-CQDs@Dox accumulation in the tumor sites at indicated time intervals. (d) FL microscopy images of the tumor sections after 12 and 24 h of post-injection of *g*-CQDs@Dox with corresponding line-scan profile. Scale bar: 100 μm. (e) *Ex vivo* biodistribution analysis of the major organs excised from the tumor-bearing mice after *g*-CQDs@Dox injection with (f) corresponding fluorescence intensities. Data are mean ± s.d. (n = 3), statistical significance at $^*p < 0.05$.

which was significantly colocalized with DAPI (blue fluorescence) in the nucleus, confirming the efficient delivery of Dox through *g*-CQDs. Therefore, our developed nanocarriers displayed good *in vivo* biocompatibility with continuous accumulation in the tumor sites through the EPR effect.[75] To evaluate the biosafety of the developed *g*-CQDs@Dox nanocarriers, the *ex vivo* fluorescence measurement of various organs (lungs, heart, liver, spleen, and kidneys) was conducted up to 24 h, and the results are shown in Fig. 9(d and e). Dox treatment had potential side effects, including cardiomyopathy, acute congestive heart failure (CHF), coronary artery syndrome, and arrhythmic conditions.[76] Therefore, excess RES trafficking of Dox may cause serious heart injuries apart from antitumor effects.[77] Our results indicate that the *g*-CQDs@Dox was accumulated in the liver after 1 h of administration, while the kidneys exhibited negligible accumulation of *g*-CQDs@Dox. However, after 3 h, the *g*-CQDs@Dox accumulation gradually decreased from the liver tissue and no observable accumulation in the spleen was found. We found an early accumulation of *g*-CQDs@Dox in the kidneys within 1 h, which reached the maximum at 3 h, and gradually decreased after 6 h of administration, followed by removal through kidneys in the form of urine. No observable accumulation in the heart was found within 24 h of administration of *g*-CQDs@Dox. These results signify that the developed nanocarrier had no potential side-effects *in vivo* and is clinically safe for anti-tumor therapy.

2.10. *In vivo* anti-tumor efficacy

Since *in vitro* and *in vivo* biosafety analysis results demonstrated beneficial effects, we investigated the *in vivo* anti-tumor efficiency of the developed probe in a subcutaneously grafted melanoma tumor model. A schematic representation of the *in vivo* experiment is shown in Fig. 10(a). The mice were randomly divided into five groups (PBS control, Dox, *g*-CQDs, and *g*-CQDs@Dox; n = 5). Dox-treated mice were used as the positive control. The anti-tumor effect was evaluated by intratumoral injection of the various formulations, and the experiment was conducted for ≤30 days. Compared to the PBS and Dox groups, the *g*-CQDs alone significantly reduced the tumor volume (~2.4 fold; $^*p < 0.05$) (Fig. 10b). Moreover, the *g*-CQDs@Dox treatment enhanced the anti-tumor efficacy by reducing tumor growth, resulting in a significant reduction in tumor volume (~21.48 fold; $^*p < 0.05$). The observed anti-tumor efficacy of *g*-CQDs@Dox is probably due to its superior targeting ability and ROS amplification, and most importantly, the cumulative release of Dox at the tumor sites. Similarly, there was a dramatic change in the tumor weight after the intratumoral injection of *g*-CQDs ($^*p < 0.05$) and *g*-CQDs@Dox ($^*p < 0.05$), compared to the control groups (Fig. 10c). Digital

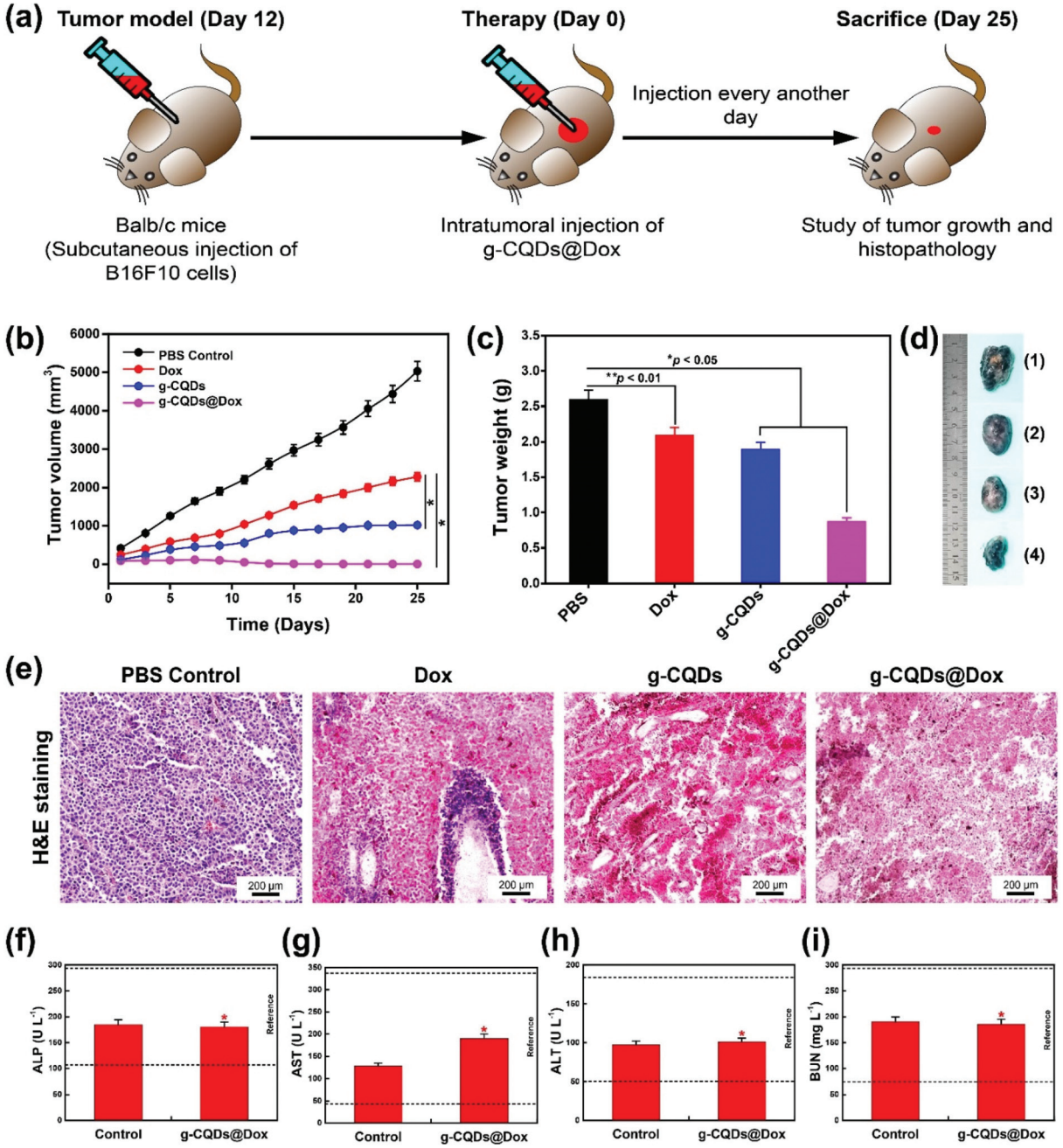

Fig. 10 *In vivo* therapeutic efficacy of *g*-CQDs and *g*-CQDs@Dox complex. (a) Schematic presentation for study design. (b) Tumor volume measurement of B16F10 tumor-bearing mice after administration of PBS, Dox, *g*-CQDs, and *g*-CQDs@Dox (n = 5). (c) Relative tumor weight of the mice after administration of PBS, Dox, *g*-CQDs, and *g*-CQDs@Dox at day 25. (d) Representative images of tumor of mice sacrificed after day 25. (1) PBS Control, (2) Dox only, (3) *g*-CQDs, and (4) *g*-CQDs@Dox (e) representative H&E staining of tumor sections after various formulations at day 25. (f–i) Blood biochemistry profile of mice after 25 days of *g*-CQDs formulation. The reference values (dotted line) for Balb/c mice were obtained from the Pathology Department, Capital Medical University, China. Data are mean ± s.d. of triplicate (n = 3) experiments, statistical significance at $*p < 0.05$ and $**p < 0.01$ (one-way ANOVA test).

photographs of the excised tumors after 25 days of treatment with various formulations are depicted in Fig. 10(d), which also show a reduced tumor size after *g*-CQD and *g*-CQDs@Dox therapy. The anti-tumor effect was further supported by H&E staining of the tumor sites after 25 days of treatment. As shown in Fig. 10e, the Dox- and *g*-CQD-treated mice showed a moderate change in histopathology, indicating higher viability of tumor cells. The PBS control group also exhibited no significant change in the morphology of the tissue. Approximately 60% of all mice from the control group died on day 20. However, the *g*-CQD and *g*-CQDs@Dox groups showed higher survival. The *g*-CQDs@Dox group exhibited the destruction of

tumor cells, mainly in the nucleus. The reduced survival may be due to the higher accumulation of Dox and *g*-CQDs in the tumor cells, leading to cell necrosis, fragmentation, and pyknosis.[78,79]

To evaluate the biosafety of the formulated compounds, we investigated the blood biochemistry and complete blood count (CBC) profile of the tumor-bearing mice after 25 days of treatment, and the results are shown in Fig. S15.† The liver/kidney function index as a function of alkaline phosphatase (ALP), aspartate aminotransferase (AST), alanine aminotransferase (ALT), and kidney urea-nitrogen index (BUN) was monitored after 25 days of treatment and showed no observable changes (Fig. 10f–i). All the parameters mentioned above were within the reference range, compared to the control groups. Notably, no noticeable abnormalities were found in any of the formulations, except a slight decrease in the RBC count in the *g*-CQDs@Dox group. Taken together, our results demonstrate that the developed *g*-CQDs@Dox complex is safe and displays less *in vivo* cytotoxicity that could be ideal for anti-tumor therapy.

3. Conclusion

In this study, we developed polyphenolic *g*-CQDs from phloroglucinol *via* a facile wet chemistry method with attractive features: highly green emissive nature, one- and two-photon excitable bioimaging property, nuclear delivery of Dox, and tumor targeting property. Dox was successfully conjugated with the *g*-CQDs *via* electrostatic interactions. The as-prepared *g*-CQDs@Dox complex was stable and exhibited excellent tumor cell-targeting properties in an acidic-pH environment. Furthermore, the one- and two-photon cell imaging revealed deep cell membrane imaging, allowing the real-time dynamic monitoring of tumor cells with excellent theranostic properties. To the best of our knowledge, this is the first report of green emissive polyphenolic CQDs with multifunctional application that could be used as a "smart" nanomaterial for tumor tracking and tumor therapy.

4. Experimental section

Details of the *g*-CQDs synthesis, *in vitro*, and *in vivo* experiments are given in the ESI.† The MDA-MB-231 (human origin, 51 years, female) and B16F10 (adult male mouse, melanoma type) cells were obtained from the American Type Culture Collection (ATCC) and Korean Cell Line Bank (KCLB), Republic of Korea. Fresh blood was obtained from 2–4 week-old Balb/c nude mice (SPF Biotechnology, Beijing, China).

Ethical statement

All animal procedures were performed in accordance with the Guidelines for Care and Use of Laboratory Animals of the Capital Medical University and experiments were approved by the Animal Ethics Committee (Permission No. KQYY-201912-003) of the Capital Medical University, Beijing, China.

Author contributions

Sayan D. Dutta: conceptualization, methodology, validation, formal analysis, writing – original draft. Jongsung Kim: validation, formal analysis, investigation, funding acquisition. Jin Hexiu: methodology, formal analysis. Sourav Sarkar: validation, formal analysis, methodology. Jagannath Mondal, Jeong Man An, and Yong-Kyu Lee: methodology, formal analysis. Md Moniruzzaman: formal analysis, writing – review and editing, project administration, supervision, validation. Ki-Taek Lim: writing – review and editing, project administration, validation, supervision, funding acquisition.

Conflicts of interest

The authors declare no competing financial or personal interests.

Acknowledgements

This work was supported by the Basic Research Program through the National Research Foundation of Korea (NRF) funded by the Ministry of Education (Grant No. 2018R1A6A1A03025582 & 2019R1D1A3A03103828). This research was also supported by the Basic Science Research Program through the National Research Foundation of Korea (NRF) funded by the Ministry of Education (Grant No. 2021R1A6A1A03038996 & 2017R1D1A1B04035070). We would also like to thank the Korea Basic Science Institute (KBSI), Chuncheon Center for the HR-TEM facility.

References

1 Y. Gao, G. Feng, T. Jiang, C. Goh, L. Ng, B. Liu, B. Li, L. Yang, J. Hua and H. Tian, *Adv. Funct. Mater.*, 2015, **25**, 2857–2866.
2 Y. Song, X. Li, S. Cong, H. Zhao and M. Tan, *Colloids Surf., B*, 2019, **180**, 449–456.
3 L. Pan, Q. He, J. Liu, Y. Chen, M. Ma, L. Zhang and J. Shi, *J. Am. Chem. Soc.*, 2012, **134**, 5722–5725.
4 M. Shi, K. Ho, A. Keating and M. S. Shoichet, *Adv. Funct. Mater.*, 2009, **19**, 1689–1696.
5 Y. Cai, H. Shen, J. Zhan, M. Lin, L. Dai, C. Ren, Y. Shi, J. Liu, J. Gao and Z. Yang, *J. Am. Chem. Soc.*, 2017, **139**, 2876–2879.
6 P. Pei, C. Sun, W. Tao, J. Li, X. Yang and J. Wang, *Biomaterials*, 2019, **188**, 74–82.
7 W. Pang, P. Jiang, S. Ding, Z. Bao, N. Wang, H. Wang, J. Qu, D. Wang, B. Gu and X. Wei, *Adv. Healthcare Mater.*, 2020, **9**, 2000607.

8 Y. Hailing, L. Xiufang, W. Lili, L. Baoqiang, H. Kaichen, H. Yongquan, Z. Qianqian, M. Chaoming, R. Xiaoshuai and Z. Rui, *Nanoscale*, 2020, **12**, 17222–17237.
9 R. Wu, J. Liu, D. Chen and J. Pan, *ACS Appl. Nano Mater.*, 2019, **2**, 4333–4341.
10 C. De La Torre, I. Casanova, G. Acosta, C. Coll, M. J. Moreno, F. Albericio, E. Aznar, R. Mangues, M. Royo and F. Sancenón, *Adv. Funct. Mater.*, 2015, **25**, 687–695.
11 A. G. Tkachenko, H. Xie, D. Coleman, W. Glomm, J. Ryan, M. F. Anderson, S. Franzen and D. L. Feldheim, *J. Am. Chem. Soc.*, 2003, **125**, 4700–4701.
12 S.-Y. Lin, N.-T. Chen, S.-P. Sun, J. C. Chang, Y.-C. Wang, C.-S. Yang and L.-W. Lo, *J. Am. Chem. Soc.*, 2010, **132**, 8309–8315.
13 S. Sindhwani, A. M. Syed, J. Ngai, B. R. Kingston, L. Maiorino, J. Rothschild, P. MacMillan, Y. Zhang, N. U. Rajesh and T. Hoang, *Nat. Mater.*, 2020, **19**, 566–575.
14 M. Zheng, S. Liu, J. Li, D. Qu, H. Zhao, X. Guan, X. Hu, Z. Xie, X. Jing and Z. Sun, *Adv. Mater.*, 2014, **26**, 3554–3560.
15 S. Li, W. Su, H. Wu, T. Yuan, C. Yuan, J. Liu, G. Deng, X. Gao, Z. Chen and Y. Bao, *Nat. Biomed. Eng.*, 2020, **4**, 704–716.
16 S. N. Baker and G. A. Baker, *Angew. Chem., Int. Ed.*, 2010, **49**, 6726–6744.
17 M. Moniruzzaman and J. Kim, *Appl. Surf. Sci.*, 2021, **552**, 149372.
18 M. Moniruzzaman, B. A. Lakshmi, S. Kim and J. Kim, *Nanoscale*, 2020, **12**, 11947–11959.
19 H. Li, Z. Kang, Y. Liu and S.-T. Lee, *J. Mater. Chem.*, 2012, **22**, 24230–24253.
20 Y. Yuan, B. Guo, L. Hao, N. Liu, Y. Lin, W. Guo, X. Li and B. Gu, *Colloids Surf., B*, 2017, **159**, 349–359.
21 J. Tang, B. Kong, H. Wu, M. Xu, Y. Wang, Y. Wang, D. Zhao and G. Zheng, *Adv. Mater.*, 2013, **25**, 6569–6574.
22 L. Yang, Z. Wang, J. Wang, W. Jiang, X. Jiang, Z. Bai, Y. He, J. Jiang, D. Wang and L. Yang, *Nanoscale*, 2016, **8**, 6801–6809.
23 D. Li, L. Lin, Y. Fan, L. Liu, M. Shen, R. Wu, L. Du and X. Shi, *Bioact. Mater.*, 2021, **6**, 729–739.
24 L. Hou, D. Chen, R. Wang, R. Wang, H. Zhang, Z. Zhang, Z. Nie and S. Lu, *Angew. Chem., Int. Ed.*, 2021, **60**, 6581–6592.
25 N. Gong, X. Ma, X. Ye, Q. Zhou, X. Chen, X. Tan, S. Yao, S. Huo, T. Zhang and S. Chen, *Nat. Nanotechnol.*, 2019, **14**, 379–387.
26 X. Gong, Q. Zhang, Y. Gao, S. Shuang, M. M. Choi and C. Dong, *ACS Appl. Mater. Interfaces*, 2016, **8**, 11288–11297.
27 S. D. Hettiarachchi, E. K. Cilingir, H. Maklouf, E. S. Seven, S. Paudyal, S. Vanni, R. M. Graham and R. M. Leblanc, *Nanoscale*, 2021, **13**, 5507–5518.
28 H. Chen, Z. Liu, B. Wei, J. Huang, X. You, J. Zhang, Z. Yuan, Z. Tang, Z. Guo and J. Wu, *Bioact. Mater.*, 2021, **6**, 655–665.
29 F. Yuan, T. Yuan, L. Sui, Z. Wang, Z. Xi, Y. Li, X. Li, L. Fan, Z. A. Tan and A. Chen, *Nat. Commun.*, 2018, **9**, 1–11.
30 L. Wang, W. Li, L. Yin, Y. Liu, H. Guo, J. Lai, Y. Han, G. Li, M. Li and J. Zhang, *Sci. Adv.*, 2020, **6**, eabb6772.
31 F. Yuan, Y.-K. Wang, G. Sharma, Y. Dong, X. Zheng, P. Li, A. Johnston, G. Bappi, J. Z. Fan and H. Kung, *Nat. Photonics*, 2020, **14**, 171–176.
32 P. Kumar, S. Senthamilselvi and M. Govindaraju, *RSC Adv.*, 2014, **4**, 26787–26795.
33 C. S. Estes, A. Y. Gerard, J. D. Godward, S. B. Hayes, S. H. Liles, J. L. Shelton, T. S. Stewart, R. I. Webster and H. F. Webster, *Carbon*, 2019, **142**, 547–557.
34 E. Fuente, J. Menéndez, M. Díez, D. Suárez and M. Montes-Morán, *J. Phys. Chem. B*, 2003, **107**, 6350–6359.
35 S. Suganuma, K. Nakajima, M. Kitano, D. Yamaguchi, H. Kato, S. Hayashi and M. Hara, *J. Am. Chem. Soc.*, 2008, **130**, 12787–12793.
36 G. Yang, X. Wan, Y. Su, X. Zeng and J. Tang, *J. Mater. Chem. A*, 2016, **4**, 12841–12849.
37 Y. Wang, D. Wang, M. Tan, B. Jiang, J. Zheng, N. Tsubaki and M. Wu, *ACS Appl. Mater. Interfaces*, 2015, **7**, 26767–26775.
38 Y. Qu, X. Xu, R. Huang, W. Qi, R. Su and Z. He, *Chem. Eng. J.*, 2020, **382**, 123016.
39 F. Yuan, Z. Wang, X. Li, Y. Li, Z. A. Tan, L. Fan and S. Yang, *Adv. Mater.*, 2017, **29**, 1604436.
40 T. Kong, L. Hao, Y. Wei, X. Cai and B. Zhu, *Cell Proliferation*, 2018, **51**, e12488.
41 W. Su, R. Guo, F. Yuan, Y. Li, X. Li, Y. Zhang, S. Zhou and L. Fan, *J. Phys. Chem. Lett.*, 2020, **11**, 1357–1363.
42 J. Li, M. Li, L. Tian, Y. Qiu, Q. Yu, X. Wang, R. Guo and Q. He, *Int. J. Pharm.*, 2020, **578**, 119122.
43 B. Zhang, Q. Duan, Y. Li, J. Wang, W. Zhang and S. Sang, *RSC Adv.*, 2021, **11**, 2656–2663.
44 P. Sarkar, S. Ghosh and K. Sarkar, *Colloids Surf., B*, 2021, **197**, 111382.
45 H.-J. Wang, T.-T. Yu, H.-L. Chen, W.-B. Nan, L.-Q. Xie and Q.-Q. Zhang, *Dyes Pigm.*, 2018, **159**, 245–251.
46 Y. Liu, W. Duan, W. Song, J. Liu, C. Ren, J. Wu, D. Liu and H. Chen, *ACS Appl. Mater. Interfaces*, 2017, **9**, 12663–12672.
47 J. Anastassopoulou and T. Theophanides, in *Bioinorganic chemistry*, Springer, 1995, pp. 209–218.
48 X. Huang, F. Zhang, L. Zhu, K. Y. Choi, N. Guo, J. Guo, K. Tackett, P. Anilkumar, G. Liu and Q. Quan, *ACS Nano*, 2013, **7**, 5684–5693.
49 T. Sun, M. Zheng, Z. Xie and X. Jing, *Mater. Chem. Front.*, 2017, **1**, 354–360.
50 N. Gao, W. Yang, H. Nie, Y. Gong, J. Jing, L. Gao and X. Zhang, *Biosens. Bioelectron.*, 2017, **96**, 300–307.
51 A. M. Sawy, A. Barhoum, S. A. A. Gaber, S. M. El-Hallouty, W. G. Shousha, A. A. Maarouf and A. S. Khalil, *Mater. Sci. Eng., C*, 2021, **122**, 111921.
52 L. Tavano, R. Muzzalupo, L. Mauro, M. Pellegrino, S. Ando and N. Picci, *Langmuir*, 2013, **29**, 12638–12646.
53 H. U. Lee, S. Y. Park, E. S. Park, B. Son, S. C. Lee, J. W. Lee, Y.-C. Lee, K. S. Kang, M. I. Kim and H. G. Park, *Sci. Rep.*, 2014, **4**, 1–7.
54 X. Cai, Y. Luo, W. Zhang, D. Du and Y. Lin, *ACS Appl. Mater. Interfaces*, 2016, **8**, 22442–22450.
55 C. Shi, D. Guo, K. Xiao, X. Wang, L. Wang and J. Luo, *Nat. Commun.*, 2015, **6**, 1–14.

56 M. Xu, G. He, Z. Li, F. He, F. Gao, Y. Su, L. Zhang, Z. Yang and Y. Zhang, *Nanoscale*, 2014, **6**, 10307–10315.
57 J. L. Griffin and J. P. Shockcor, *Nat. Rev. Cancer*, 2004, **4**, 551–561.
58 E. Persi, M. Duran-Frigola, M. Damaghi, W. R. Roush, P. Aloy, J. L. Cleveland, R. J. Gillies and E. Ruppin, *Nat. Commun.*, 2018, **9**, 1–11.
59 D. Trachootham, J. Alexandre and P. Huang, *Nat. Rev. Drug Discovery*, 2009, **8**, 579–591.
60 P. Swietach, R. D. Vaughan-Jones and A. L. Harris, *Cancer Metastasis Rev.*, 2007, **26**, 299–310.
61 M. J. Boyer and I. F. Tannock, *Cancer Res.*, 1992, **52**, 4441–4447.
62 A. Banstola, K. Poudel, S. Pathak, P. Shrestha, J. O. Kim, J.-H. Jeong and S. Yook, *ACS Appl. Mater. Interfaces*, 2021, **13**(19), 22955–22969.
63 Y. Chong, Y. Ma, H. Shen, X. Tu, X. Zhou, J. Xu, J. Dai, S. Fan and Z. Zhang, *Biomaterials*, 2014, **35**, 5041–5048.
64 Z. Kong, W. Hu, F. Jiao, P. Zhang, J. Shen, B. Cui, H. Wang and L. Liang, *J. Phys. Chem. B*, 2020, **124**, 9335–9342.
65 G. E. Kellogg, J. N. Scarsdale and F. A. Fornari Jr., *Nucleic Acids Res.*, 1998, **26**, 4721–4732.
66 R. C. Calizo, S. Bhattacharya, J. C. van Hasselt, C. Wei, J. S. Wong, R. J. Wiener, X. Ge, N. J. Wong, J.-J. Lee and C. M. Cuttitta, *Nat. Commun.*, 2019, **10**, 1–15.
67 J. Ma, K. Kang, Y. Zhang, Q. Yi and Z. Gu, *ACS Appl. Mater. Interfaces*, 2018, **10**, 43923–43935.
68 K. Li, Y. Lyu, Y. Huang, S. Xu, H.-W. Liu, L. Chen, T.-B. Ren, M. Xiong, S. Huan and L. Yuan, *Proc. Natl. Acad. Sci. U. S. A.*, 2021, **118**, 1–10.
69 S. Yi, S. Deng, X. Guo, C. Pang, J. Zeng, S. Ji, H. Liang, X.-C. Shen and B.-P. Jiang, *Carbon*, 2021, **182**, 155–166.
70 G. Han, J. Zhao, R. Zhang, X. Tian, Z. Liu, A. Wang, R. Liu, B. Liu, M. Y. Han and X. Gao, *Angew. Chem.*, 2019, **131**, 7161–7165.
71 Z.-J. Zhu, Y.-C. Yeh, R. Tang, B. Yan, J. Tamayo, R. W. Vachet and V. M. Rotello, *Nat. Chem.*, 2011, **3**, 963–968.
72 E. Muro, A. Fragola, T. Pons, N. Lequeux, A. Ioannou, P. Skourides and B. Dubertret, *Small*, 2012, **8**, 1029–1037.
73 J. Shao, H. Xie, H. Huang, Z. Li, Z. Sun, Y. Xu, Q. Xiao, X.-F. Yu, Y. Zhao and H. Zhang, *Nat. Commun.*, 2016, **7**, 1–13.
74 V. Torchilin, *Adv. Drug Delivery Rev.*, 2011, **63**, 131–135.
75 K. Yang, J. Wan, S. Zhang, Y. Zhang, S.-T. Lee and Z. Liu, *ACS Nano*, 2011, **5**, 516–522.
76 S. Upadhyay, K. B. Gupta, A. K. Mantha and M. Dhiman, *J. Cell. Biochem.*, 2021, **122**, 153–165.
77 K. M. Huang, M. Z. Thomas, T. Magdy, E. D. Eisenmann, M. E. Uddin, D. F. DiGiacomo, A. Pan, M. Keiser, M. Otter and S. H. Xia, *Proc. Natl. Acad. Sci. U. S. A.*, 2021, **118**, 1–9.
78 H. Alizadeh, M. S. Pidherney, J. P. McCULLEY and J. Y. Niederkorn, *Infect. Immun.*, 1994, **62**, 1298–1303.
79 X. Yang, G. Chen, K. N. Yu, M. Yang, S. Peng, J. Ma, F. Qin, W. Cao, S. Cui and L. Nie, *Cell Death Dis.*, 2020, **11**, 1–11.